The evolution of the star formation rate function and cosmic star formation rate density of galaxies at z ˜ 1-4

Article (Published Version)

Monthly Notices
of the
ROYAL ASTRONOMICAL SOCIETY

MNRAS **464,** 4977–4994 (2017)
Advance Access publication 2016 October 18

doi:10.1093/mnras/stw2680

The evolution of the star formation rate function and cosmic star formation rate density of galaxies at $z \sim 1$–4

A. Katsianis,[1,3]★ E. Tescari,[2,3] G. Blanc[1] and M. Sargent[4]

[1]*Department of Astronomy, Universitad de Chile, Camino El Observatorio 1515, Las Condes, 7591245 Santiago, Chile*
[2]*School of Physics, The University of Melbourne, Parkville, VIC 3010, Australia*
[3]*ARC Centre of Excellence for All-Sky Astrophysics (CAASTRO), The University of Sydney, NSW 2006, Australia*
[4]*Astronomy Centre, Department of Physics and Astronomy, University of Sussex, Brighton BN1 9QH, UK*

Accepted 2016 October 14. Received 2016 October 12; in original form 2016 June 16

ABSTRACT

We investigate the evolution of the galaxy star formation rate function (SFRF) and cosmic star formation rate density (CSFRD) of $z \sim 1$–4 galaxies, using cosmological smoothed particle hydrodynamic (SPH) simulations and a compilation of ultraviolet (UV), infrared (IR) and Hα observations. These tracers represent different populations of galaxies with the IR light being a probe of objects with high star formation rates and dust contents, while UV and Hα observations provide a census of low star formation galaxies where mild obscuration occurs. We compare the above SFRFs with the results of SPH simulations run with the code P-GADGET3(XXL). We focus on the role of feedback from active galactic nuclei (AGN) and supernovae in form of galactic winds. The AGN feedback prescription that we use decreases the simulated CSFRD at $z < 3$ but is not sufficient to reproduce the observed evolution at higher redshifts. We explore different wind models and find that the key factor for reproducing the evolution of the observed SFRF and CSFRD at $z \sim 1$–4 is the presence of a feedback prescription that is prominent at high redshifts ($z \geq 4$) and becomes less efficient with time. We show that variable galactic winds which are efficient at decreasing the SFRs of low-mass objects are quite successful in reproducing the observables.

Key words: galaxies: evolution – galaxies: formation – galaxies: luminosity function, mass function – galaxies: star formation – galaxies: statistics – cosmology: theory.

1 INTRODUCTION

The star formation rates (SFRs) of galaxies represent a fundamental constraint for galaxy formation models. The basic idea for calculating the average SFR of an object is to estimate the number of young bright stars with a certain age. However, in most cases, especially at high redshifts, galaxies are not spatially resolved and there is only access to their integrated spectrum. Hence, to quantify the SFRs of galaxies, we typically rely on the observed luminosities and luminosity functions (LFs; Madau & Dickinson 2014). Some typical SFR indicators are the following.

(i) Ultraviolet (UV) luminosity: the main advantage of the UV luminosity is that it gives a direct estimate of the young stellar population since both O and B stars are brighter in the UV than at longer wavelengths. Furthermore, at high redshifts ($z \geq 4$) only the UV emission from galaxies is observable with the current instrumentation. The simplest method of obtaining the SFR of an object is to assume a linear scaling between the SFR and the continuum luminosity integrated over a fixed band in the blue or near-ultraviolet (NUV). The optimal wavelength range is 1500–2800 Å (Kennicutt 1998b; Smit et al. 2012). Evolutionary synthesis models provide relations between the SFR per unit mass, luminosity and the integrated colour of the population. The conversion between the UV luminosity and SFR (Kennicutt 1998b; Smit et al. 2012) is found from these models to be

$$\mathrm{SFR_{UV}}\,(\mathrm{M_\odot\,yr^{-1}}) = 1.4 \times 10^{-28}\ L_{\mathrm{UV}}\,(\mathrm{erg\,s^{-1}\,Hz^{-1}}), \quad (1)$$

where L_{UV} is the UV luminosity of galaxies. The relation is valid from 1500 to 2800 Å and assumes a Salpeter (1955) initial mass function (IMF). From $z \sim 0.5$ to $z \sim 3$, the majority of star formation took place in obscured and dusty environments and most of the UV photons were reprocessed by dust into infrared (IR) emission (Le Floc'h et al. 2005; Dole et al. 2006; Rujopakarn et al. 2011). Therefore, a dust correction is required.

(ii) Hα luminosity and nebular emission lines: the other SFR indicators to be discussed in this paper rely on measuring light from young, massive stars that have been reprocessed by interstellar gas or dust. O and B stars produce large amounts of UV photons that

★ E-mail: kata@das.uchile.cl

ionize the surrounding gas. Hydrogen recombination produces line emission, including the Balmer series lines like Hα (6562.8 Å) and H β (4861.2 Å). Other nebular emission lines from other elements, like [O II] (Kewley, Geller & Jansen 2004) and [O III] (Teplitz et al. 2000; Moustakas, Kennicutt & Tremonti 2006) can be used to infer the number of blue massive stars ([O III] lines are known to be very sensitive to the ionization parameter so [O II] is typically preferred between them as an SFR indicator). Probing the existence of massive stars using the Hα luminosity of an object is quite common in the literature (Kennicutt 1983; Gallego et al. 1995; Kennicutt 1998b; Pettini et al. 1998; Glazebrook et al. 1999; Hopkins, Connolly & Szalay 2000; Moorwood et al. 2000; Sullivan et al. 2000; Tresse et al. 2002; Pérez-González et al. 2003; Yan, Windhorst & Cohen 2003; Hanish et al. 2006; Bell et al. 2007; Ly et al. 2011; Sobral et al. 2013), since Hα photons originate from the gas ionized by the radiation of these stars. Typically, these lines trace stars with masses greater than $\sim$15 $M_{\odot}$, with the peak contribution from stars in the range 30–40 $M_{\odot}$. According to the synthesis models of Kennicutt (1998a), the relation between SFR and Hα luminosity is the following:

$$\mathrm{SFR}_{\mathrm{H}\alpha}\,(M_{\odot}\,\mathrm{yr}^{-1}) = 7.9\times10^{-42}\ L_{\mathrm{H}\alpha}\,(\mathrm{erg\,s}^{-1}), \quad (2)$$

where $L_{\mathrm{H}\alpha}$ is the Hα luminosity of the galaxies. While it is desirable to extend Hα studies to higher redshifts, such task is typically observationally difficult because most of the Hα luminosity is redshifted into the IR beyond $z \sim 0.4$.

(iii) The IR luminosity originating from dust continuum emission is a star formation indicator and a good test of dust physics (Hirashita, Buat & Inoue 2003). The shape of the thermal IR light depends on a lot of parameters (Draine & Li 2007) like the dust opacity index, dust temperature, strength of the interstellar radiation field and polycyclic aromatic hydrocarbon abundance, in the sense that UV-luminous, young stars will heat the dust to higher temperatures than older stellar populations (Helou 1986). The dust (heated by UV-luminous and young stellar populations) produces an IR spectral distribution that is more luminous than the one produced by low-mass stars. This is the foundation for using the IR emission($\sim$5–1000 μm) as a probe of UV-bright stars and an SFR indicator. There are two approaches to study the SFR using IR observations. Both involve IR photometry as a tracer of IR luminosity, which in turn traces the number of UV photons from the short-lived massive stars and allows the SFR to be calculated (Kennicutt 1998b; Rujopakarn et al. 2011). The first approach involves multiband IR photometry and constrains the total IR luminosity (Elbaz et al. 2010; Rex et al. 2010), while the second exploits just a monochromatic IR luminosity (Calzetti et al. 2007, IR at 24 μm) that correlates strongly with SFR. The relation between the SFR and total IR luminosity from the evolutionary synthesis model of Kennicutt (1998a) is found to be

$$\mathrm{SFR}_{\mathrm{IR}}\,(M_{\odot}\,\mathrm{yr}^{-1}) = 1.72\times10^{-10}\ L_{\mathrm{IR}}\,/\mathrm{L}_{\odot}. \quad (3)$$

There has been a considerable effort to constrain the evolution of the cosmic star formation rate density (CSFRD) in the last decade(Madau & Dickinson 2014). However, Ly et al. (2011) state that it is important to explore the extent to which systematics between different SFR indicators can affect its measurements. This can be done by comparing the SFRFs obtained from different indicators. In particular, it is useful to trace the star formation history with a single indicator throughout time, and then compare the overall histories from various SFR tracers.

The evolution of the SFRF has been studied by means of hydrodynamic simulations (Davé, Oppenheimer & Finlator 2011; Tescari et al. 2014) and semi-analytic modelling (Fontanot et al. 2012). Davé et al. (2011) used a set of simulations run with an improved version of GADGET-2 to study the growth of galaxies from $z \sim 0$–3. The authors investigated the effect of four different wind models and compared the simulated star formation rate functions (SFRFs) with observations (Martin 2005; Hayes, Schaerer & Östlin 2010; Ly et al. 2011). Their galactic wind models are responsible for the shape of the faint-end slope of the SFR function at $z = 0$. However, the simulations overproduce the number of objects at all SFRs. According to the authors, this tension is due to the absence of active galactic nuclei (AGN) feedback in their models.

This paper is the fourth of a series in which we present the results of the AustraliaN GADGET-3 early Universe Simulations (ANGUS) project and the observed SFRF of $z \sim$ 1–4 galaxies, that were obtained from a compilation of UV, Hα and IR LF. The aim of the ANGUS project is to study the interplay between galaxies and the intergalactic medium from intermediate redshifts ($z \sim 1$) to the epoch of reionization at $z \sim 6$ and above. We use the hydrodynamic code P-GADGET3(XXL), which is an improved version of GADGET-3 (Springel 2005). For the first time we combine physical processes, which have been developed and tested separately. In particular, our code includes:

(i) a subgrid star formation model (Springel & Hernquist 2003),
(ii) supernova energy- and momentum-driven galactic winds (Springel & Hernquist 2003; Barai et al. 2013; Puchwein & Springel 2013),
(iii) AGN feedback (Springel et al. 2005; Fabjan et al. 2010; Planelles et al. 2013),
(iv) self-consistent stellar evolution and chemical enrichment modelling (Tornatore et al. 2007b),
(v) metal-line cooling (Wiersma, Schaye & Smith 2009),
(vi) transition of metal-free Population III to Population II star formation (Tornatore, Ferrara & Schneider 2007a),
(vii) a low-viscosity smoothed particle hydrodynamic scheme to allow the development of turbulence within the intracluster medium (Dolag et al. 2005),
(viii) low-temperature cooling by molecules/metals (Maio et al. 2007),
(ix) thermal conduction (Dolag et al. 2004),
(x) passive magnetic fields based on Euler potentials (Dolag & Stasyszyn 2009),
(xi) adaptive gravitational softening (Iannuzzi & Dolag 2011).

Simulations based on the same code have also been used to successfully explore the origin of cosmic chemical abundances (Maio & Tescari 2015). In Tescari et al. (2014), we constrained and compared our numerical results with observations of the SFRF at $z \sim$ 4–7 (Smit et al. 2012). In addition, we showed that a fiducial model with strong-energy-driven winds and AGN feedback which starts to be effective at high redshifts ($z \geq 4$) is needed to obtain the observed SFRF of high-redshift galaxies. In this work, we extend the analysis to lower redshifts ($1 \leq z \leq 4$) using the same set of cosmological simulations. We explore various feedback prescriptions and investigate how these shape the galaxy SFRF. We do not investigate the broad possible range of simulations, but concentrate on the simulations that can describe the high-z SFR function (Tescari et al. 2014), galaxy stellar mass function (GSMF) and SFR$-M_{\star}$ relations (Katsianis, Tescari & Wyithe 2015, 2016).

This paper is organized as follows. In Section 2, we present the compilation of the observed LFs and dust correction laws used for this work. In Section 3, we present the observed SFRF of galaxies at $z \sim$ 1–4. In Section 4, we present a brief description of our

simulations along with the different feedback models used. In Section 5, we compare the simulated SFRFs with the constraints from the observations. In Section 6, we present the evolution of the CSFRD of the Universe in observations and simulations. Finally, in Section 7 we summarize our main results and conclusions.

2 THE OBSERVED STAR FORMATION RATES FROM GALAXY LUMINOSITIES

2.1 Dust attenuation effects and dust correction prescriptions

We correct the UV LFs for the effects of dust attenuation using the correlation of extinction with the UV-continuum slope β following Hao et al. (2011) and Smit et al. (2012). Like Smit et al. (2012), we assume the infrared excess (IRX)–β relation of Meurer et al. (1999):

$$A_{1600} = 4.43 + 1.99\,\beta, \tag{4}$$

where A_{1600} is the dust absorption at 1600 Å. We assume as well the linear relation between the UV-continuum slope β and luminosity of Bouwens et al. (2012):

$$\langle\beta\rangle = \frac{\mathrm{d}\beta}{\mathrm{d}M_{\mathrm{UV}}}\left(M_{\mathrm{UV,AB}} + 19.5\right) + \beta_{M_{\mathrm{UV}}=-19.5}. \tag{5}$$

Then following Hao et al. (2011), we assume

$$L_{\mathrm{UV_{OBS}}} = L_{\mathrm{UV_{corr}}} e^{-\tau_{\mathrm{UV}}}, \tag{6}$$

where τ_{UV} is the effective optical depth ($\tau_{\mathrm{UV}} = A_{1600}/1.086$). We calculate A_{1600} and τ_{UV} adopting the parameters for $\frac{\mathrm{d}\beta}{\mathrm{d}M_{\mathrm{UV}}}$ from Reddy & Steidel (2009), Bouwens et al. (2009, 2012) and Tacchella, Trenti & Carollo (2013).

For the case of Hα emission, Sobral et al. (2013) used the 1 mag correction which is a simplification that normally is acceptable for low redshifts ($0.0 < z < 0.3$). Ly et al. (2011) use the SFR-dependent dust correction from Hopkins et al. (2001). As mentioned above, no dust corrections are required for IR LFs.

2.2 The observed UV, IR and Hα luminosity functions from $z \sim 3.8$ to $z \sim 0.8$

To retrieve the SFRF for redshift $z \sim 3.8$ to $z \sim 0.8$, we use the LFs from Reddy et al. (2008, bolometric-UV+IR), van der Burg, Hildebrandt & Erben (2010, Lyman-break selected), Oesch et al. (2010, Lyman-break selected), Ly et al. (2011, Hα selected), Cucciati et al. (2012, *I*-band selected-flux limited), Gruppioni et al. (2013, IR selected), Magnelli et al. (2011, 2013, IR selected), Sobral et al. (2013, Hα selected), Alavi et al. (2014, Lyman-break selected) and Parsa et al. (2016, Lyman-break selected). In addition, we compare our results with the work of Smit et al. (2012) for Lyman-break selected galaxies at redshift $z \sim 3.8$. We choose the above surveys since all of them combined are ideal to study the SFRF in a large range of SFRs and redshifts. The authors have publicly available the LFs of their samples which are summarized below.

Reddy et al. (2008) used a sample of Lyman-break selected galaxies at redshifts $z \sim 2.3$ and $z \sim 3.1$, combined with ground-based spectroscopic Hα and *Spitzer* MIPS 24 μm data, and obtained robust measurements of the rest-frame UV, Hα and IR LFs. These LFs were corrected for incompleteness and dust attenuation effects. The stepwise bolometric LF of Reddy et al. (2008) is in table 9 of their work.

van der Burg et al. (2010) studied ∼ 100 000 Lyman-break galaxies from the Canada–France–Hawaii Telescope Legacy Survey at $z \sim 3.1$, 3.8, 4.8 and estimated their rest-frame 1600 Å LF. Due to the large survey volume, the authors state that cosmic variance had a negligible impact on their determination of the UV LF, allowing them to study the bright end with great statistical accuracy. They obtained the rest-frame UV LF in absolute magnitudes at 1600 Å for redshifts $z \sim 3.1$, 3.8, 4.8 and their results are in table 1 of their work.

Oesch et al. (2010) investigated the evolution of the UV LF at $z \sim 0.75$–2.5. The authors suggested that UV-colour and photometric selection have similar results for the LF in this redshift interval and claim that UV-dropout samples are well defined and reasonably complete. The authors note that the characteristic luminosity decreased by a factor of ∼16 from $z \sim 3$ to $z \sim 0$ while the faint-end slope α increased from $\alpha \sim -1.5$ to $\alpha \sim -1.2$. The parameters of the analytic expressions of the above UV LFs are provided in table 1 of Oesch et al. (2010).

Ly et al. (2011) obtained measurements of the Hα LF for galaxies at $z \sim 0.8$, based on 1.18 μm narrow-band imaging from the New Hα Survey. The authors applied corrections for dust attenuation effects and incompleteness. To correct for dust attenuation, they adopted a luminosity-dependent extinction relation following Hopkins et al. (2001). The authors applied corrections for [N II] flux contamination and the volume, as a function of line flux. The Hα LF from Ly et al. (2011) is presented in table 3 of their work.

Cucciati et al. (2012) investigated the evolution of the far-ultraviolet (FUV) and NUV LFs from $z \sim 0.05$ to $z \sim 4.5$. Using these data, they derived the CSFRD history and suggested that it peaks at $z \sim 2$ as it increases by a factor of ∼6 from $z \sim 4.5$. We use the FUV LFs to obtain an estimate of the SFRs of small galaxies. The analytic expressions of the above FUV LFs are provided in table 1 of Cucciati et al. (2012).

Gruppioni et al. (2013) used the 70-, 100-, 160-, 250-, 350- and 500-μm data from the *Herschel* surveys, PEP and HerMES, in the GOODS-S and -N, ECDFS and COSMOS fields, to characterize the evolution of the IR LF for redshifts $z \sim 4$ to $z \sim 0$. The highest redshift results of Gruppioni et al. (2013) provide some information on the bright end of the LF for high redshifts. The authors provide more useful constraints at lower redshift where IR LFs can probe low star-forming objects. The total IR LF of Gruppioni et al. (2013) is in table 6 of their work.

Magnelli et al. (2011, 2013) combined observations of the GOODS fields from the PEP and GOODS-*Herschel* programmes. From the catalogues of these fields, they derived number counts and obtained the IR LFs down to $L_{\mathrm{IR}} = 10^{11}\,\mathrm{L}_{\odot}$ at $z \sim 1$ and $L_{\mathrm{IR}} = 10^{12}\,\mathrm{L}_{\odot}$ at $z \sim 2$. The authors state that their far-IR observations provide a more accurate IR luminosity estimation than the mid-IR observations from *Spitzer*. The results of Magnelli et al. (2013) are presented in the appendix of their work.

Sobral et al. (2013) presented the combination of wide and deep narrow-band Hα surveys using United Kingdom Infrared Telescope, Subaru and the VLT. The authors robustly selected a total of 1742, 637, 515 and 807 Hα emitters across the COSMOS and the UDS fields at $z = 0.40$, 0.84, 1.47 and 2.23, respectively. These Hα LFs have then been corrected for incompleteness, [N II] contamination and for dust extinction using $A_{\mathrm{H}\alpha} = 1$ mag correction.[1] The stepwise

[1] Hopkins et al. (2001) note that an SFR-dependent dust attenuation law produces similar corrections with the 1 mag simplification often assumed for local populations. At higher redshifts ($z > 0.3$) though, larger corrections are required.

determination of the Hα LF from Sobral et al. (2013) can be found in table 4 of their work.

Alavi et al. (2014) targeted the cluster Abell 1689, behind which they searched for faint star-forming galaxies at redshift $z \sim 2$. Their data are corrected for incompleteness and dust attenuation effects. They extended the UV LF at $z \sim 2$ to very faint magnitude limits and this allowed them to constrain the α parameter of the Schechter function fit, finding that $\alpha = -1.74 \pm 0.08$. The parameters of the UV LF found with this method are in table 3 of Alavi et al. (2014).

Parsa et al. (2016) present measurements of the evolving rest-frame UV (1500 Å) galaxy LF over the redshift range $z \sim 2$–4. The results are provided by combining the HUDF, CANDELS/GOODS-South and UltraVISTA/COSMOS surveys and are able to successfully probe the faint end of the UV LF. An interesting result of the analysis is that the LF appears to be significantly shallower ($\alpha = -1.32$) than previous measurements (e.g. Alavi et al. 2014). The stepwise determination of the LF found by this method is in table 1 of Parsa et al. (2016).

2.3 The luminosity–SFR conversion

To obtain the SFRF of galaxies, we start from the observed LF. We convert the luminosities to SFRs at each bin of the LF following a method similar to the one adopted by Smit et al. (2012). UV-selected samples provide information about the SFRF of galaxies at redshifts $z > 2$. For lower redshifts they provide key constraints for low star-forming objects (faint end of the distribution), but are unable to probe dusty high star-forming systems, and thus are uncertain at the bright end of the distribution. This is due to the fact that dust corrections are insufficient or that UV-selected samples do not include a significant number of massive, dusty objects. Using IR-selected samples, we obtain SFRFs that are not affected by dust attenuation effects. However, small faint galaxies do not have enough dust to reprocess the UV light to IR, so IR luminosities do not probe the faint end of the SFRF. The observed Hα data used for this work provide us with information about the SFRF of intermediate $1.0 \leq \log(\mathrm{SFR}/(\mathrm{M}_{\odot}\,\mathrm{yr}^{-1})) \leq 2.0$ galaxies from $z \sim 0.8$ to $z \sim 2.3$. Dust corrections are required to obtain the intrinsic SFRs from Hα luminosities. We note that various authors have often published their data in the form of UV, IR or Hα LFs. However, the authors used their results to directly obtain the CSFRD instead of SFRFs since the first is known to be dominated mostly by galaxies around the characteristic luminosity. The different groups are aware of the potential problems (e.g. uncertainty in treatment of dust) that may occur when they calculate SFRs from a range of individual galaxy luminosities or bins of LFs.

3 THE OBSERVED STAR FORMATION RATE FUNCTIONS FROM $z \sim 3.8$ TO $z \sim 0.8$

3.1 The star formation rate function at $z \sim 3.8$

To obtain the SFRF at $z \sim 4$, we start with the UV LF from van der Burg et al. (2010, $z \sim 3.8$). We use the dust corrections laws of Meurer et al. (1999) and Hao et al. (2011) and obtain the dust-corrected UV LFs. We assume the same $\langle\beta\rangle$ as Smit et al. (2012) that can be found in Bouwens et al. (2012, $\langle\beta\rangle = -0.11(M_{\mathrm{UV,\,AB}} + 19.5) - 2.00$ at $z \sim 3.8$). We apply equation (1) (Kennicutt 1998a; Madau, Pozzetti & Dickinson 1998), which assumes a Salpeter (1955) IMF and convert the UV luminosities to SFRs. The blue triangles in the top left panel of Fig. 1 are the stepwise determinations of the SFRF for redshift $z \sim 3.8$ using the above method. The red triangles are the stepwise determination of the SFRF for $z \sim 3.8$ from Smit et al. (2012). The results from our analysis and those of Smit et al. (2012) imply that the UV LFs from Bouwens et al. (2007) and van der Burg et al. (2010) are consistent with each other for $z \sim 4$. The error bars of the SFRF that relies on the results of van der Burg et al. (2010) are smaller, due to less cosmic variance within the larger area covered by these observations. We use the same method to convert the UV LF of Parsa et al. (2016, $z \sim 3.8$) to a stepwise SFRF. However, the SFRF that was obtained from the UV LF of Parsa et al. (2016) has a shallower faint end. The results of Parsa et al. (2016) include fainter sources and thus provide further information for low star-forming objects. The SFRFs from our analysis for $z \sim 3.8$ are in the top left panel of Fig. 1 and Table 2. In addition, we use the IR LF from Gruppioni et al. (2013) for redshifts $3.0 < z < 4.2$. We convert the IR luminosities to SFRs using equation (3). We see that the IR luminosity is unable to provide information for a broad population of $z \sim 4$ galaxies and is only a census of objects with very high SFRs. Thus, unlike UV LFs, rest-frame IR studies are not suitable for constraining the SFRF and CSFRD at high redshifts.

3.2 The star formation rate function at $z \sim 3.1$

To obtain the SFRF at redshift $z \sim 3.1$, we start with the UV LF from van der Burg et al. (2010, $z \sim 3.1$) and Parsa et al. (2016, $z \sim 3.0$). We follow the same procedure described above. We assume the $\langle\beta\rangle$ relations from Reddy & Steidel (2009) that can be found in Tacchella et al. (2013) who show $\langle\beta\rangle = -0.13(M_{\mathrm{UV,AB}} + 19.5) - 1.85$ at $z \sim 3.0$. The blue triangles in the top right panel of Fig. 1 are the stepwise determination of the SFRF for redshift $z \sim 3.1$ using the UV LF of van der Burg et al. (2010), while the grey squares are the SFRF from Parsa et al. (2016). In addition, we use the bolometric LF from Reddy et al. (2008, $z \sim 2.7$–3.4). This LF is already corrected for incompleteness and dust attenuation effects. To obtain the SFRF from the bolometric LF, we use equation (3). The orange filled circles in the top right panel of Fig. 1 are the stepwise determination of the SFRF for $z \sim 3.1$ using the above procedure.

We see that the SFRFs we obtain using the data of Reddy et al. (2008), van der Burg et al. (2010) and Parsa et al. (2016) are in good agreement. The SFRF we retrieve employing the LF of Parsa et al. (2016) can probe objects with low SFRs and thus provide better constraints for the small objects in our simulations. The red diamonds are obtained using the IR data of Gruppioni et al. (2013) for $z \sim 2.5$–3.0 and will be discussed in detail in the next section. The results for $z \sim 3.1$ are summarized in Table 3 and the top right panel of Fig. 1.

3.3 The star formation rate function at $z \sim 2.6$

To obtain the SFRF for $z \sim 2.6$ galaxies, we use the bolometric data of Reddy et al. (2008) at $z \sim 1.9$–3.4, the Schechter fit of the UV LF of Oesch et al. (2010, $z \sim 2.5$) and the IR LF of Gruppioni et al. (2013) at $z \sim 2.5$–3.0. To convert the LF of Oesch et al. (2010), we assume the $\langle\beta\rangle$ relations from Bouwens et al. (2009, 2012) who find $\langle\beta\rangle = -0.20(M_{\mathrm{UV,AB}} + 19.5) - 1.70$ at $z \sim 2.5$. The results of this analysis are shown in the bottom left panel of Fig. 1 (green dotted line). Moreover, we use equation (3) to convert the IR luminosities of Gruppioni et al. (2013) to SFRs. The SFRF from the IR LF is only able to constrain the SFRs of luminous star-forming systems at this high redshift. However, they indicate that the UV SFRs that are

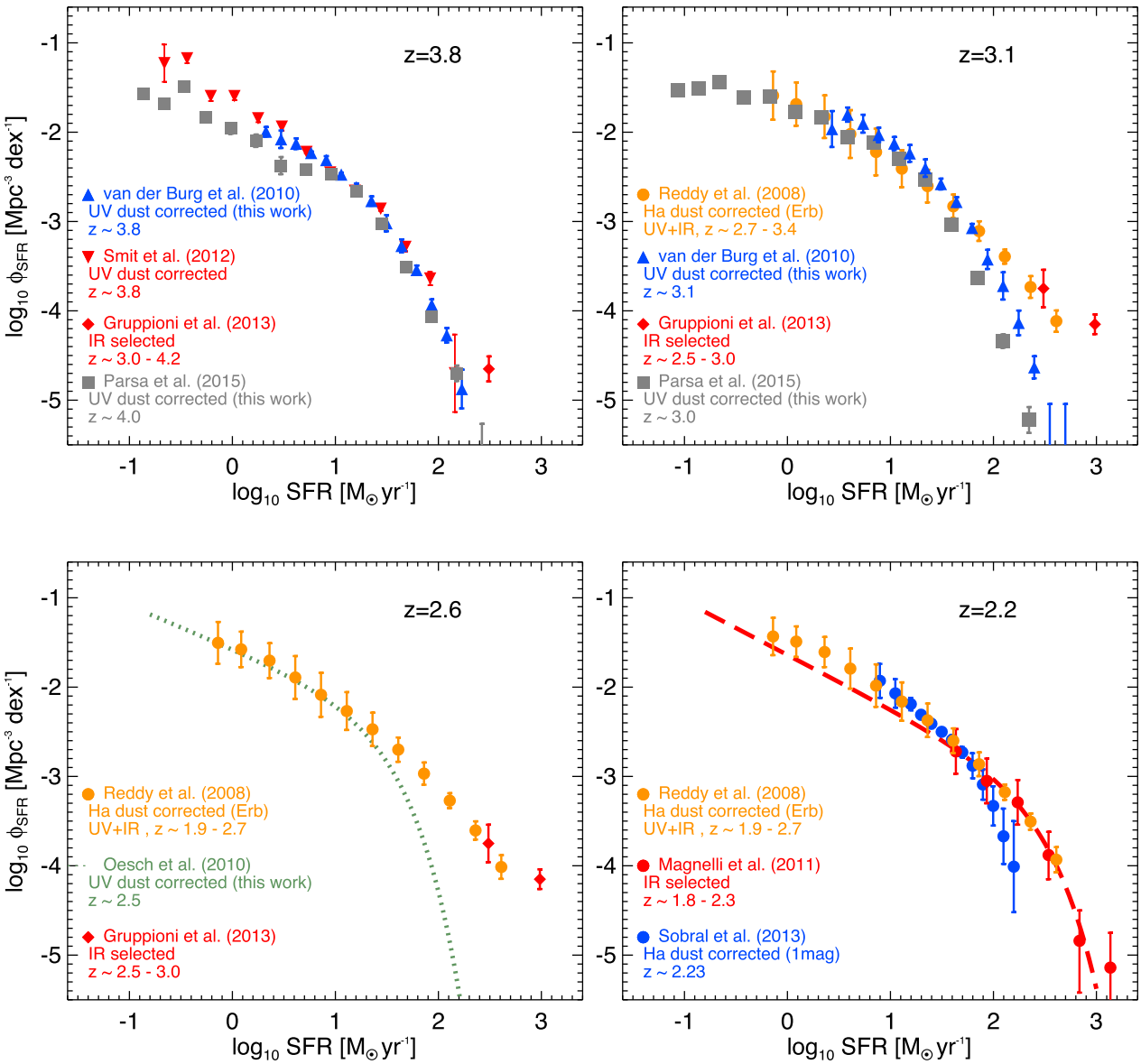

Figure 1. The stepwise and analytical determinations of the observed SFRF for redshifts $z \sim 3.8$ (top left panel), $z \sim 3.1$ (top right panel), $z \sim 2.6$ (bottom left panel) and $z \sim 2.2$ (bottom right panel). The blue filled circles are the SFRFs for $z \sim 2.2$ using the Hα LF from Sobral et al. (2013). The red filled circles and red dashed line are the SFRFs for redshift $z \sim 2.2$ using the IR LF from Magnelli et al. (2011). The red filled diamonds are the SFRF for redshifts $z \sim 2.6$, $z \sim 3.1$ and $z \sim 3.8$ using the IR LF from Gruppioni et al. (2013). The orange filled circles are the SFRF for redshifts $z \sim 2.2$, $z \sim 2.6$ and $z \sim 3.1$ using the bolometric LF from Reddy et al. (2008). The green dotted line is the analytic SFRF obtained using the results of Oesch et al. (2010). The blue triangles at $z \sim 3.1$ and $z \sim 3.8$ were retrieved from dust correcting the UV LFs of van der Burg et al. (2010). For the grey squares, we used the UV LF from Parsa et al. (2016). The red inverted triangles are the stepwise determination of the SFRF at $z \sim 3.8$ from Smit et al. (2012).

obtained from IRX–β relation are underestimated or the Lyman-break selected sample of Oesch et al. (2010) misses a significant number of high star-forming systems. The results for $z \sim 2.6$ are summarized in Table 4 and the bottom left panel of Fig. 1.

3.4 The star formation rate function at $z \sim 2.2$

To obtain the SFRF at redshift $z \sim 2.2$, we use the LFs of Reddy et al. (2008, $z \sim 1.9$–2.7), Magnelli et al. (2011, $z \sim 1.8$–2.3) and Sobral et al. (2013, $z \sim 2.23$). The orange filled circles in the bottom right panel of Fig. 1 represent the stepwise determination of the SFRF for redshift $z \sim 2.2$ using the bolometric LF at $z \sim 2.3$ from Reddy et al. (2008) and equation (3). In addition, we use the Hα LF from Sobral et al. (2013). As discussed in Section 2.2, this LF is corrected for incompleteness and dust attenuation effects (1 mag simplification). To obtain the SFRF from the Hα LF we use equation (2). The blue filled circles of Fig. 1 are the stepwise determination of the SFRF for $z \sim 2.2$ using the above analysis.

Table 1. The dust correction formulas used for the UV, IR and Hα luminosities in this work.

SFR indicator	Dust corrections
UV	Meurer, Heckman & Calzetti (1999) and Hao et al. (2011)
IR	No dust corrections needed
Hα	1 mag, Hopkins et al. (2001)

Table 2. Stepwise SFR functions at $z \sim 3.8$ using the data from van der Burg et al. (2010, blue triangles in the top left panel of Fig. 1), Gruppioni et al. (2013, red diamonds in the top left panel of Fig. 1) and Parsa et al. (2016, grey squares in the top left panel of Fig. 1).

$\log \frac{\mathrm{SFR}}{\mathrm{M}_\odot\ \mathrm{yr}^{-1}}$	$\log \phi_{\mathrm{SFR}}\ (\mathrm{Mpc}^{-3}\ \mathrm{dex}^{-1})$
$z \sim 3.8$, (Parsa et al. 2016, UV)	Dust corrected
−0.86	-1.57 ± 0.03
−0.66	-1.68 ± 0.04
−0.47	-1.49 ± 0.03
−0.26	-1.83 ± 0.05
−0.02	-1.96 ± 0.06
0.23	-2.10 ± 0.07
0.47	-2.37 ± 0.10
0.72	-2.42 ± 0.28
0.96	-2.47 ± 0.03
1.20	-2.66 ± 0.04
1.45	-3.02 ± 0.01
1.69	-3.51 ± 0.03
1.93	-4.07 ± 0.05
2.18	-4.70 ± 0.09
2.42	-5.70 ± 0.43
$\langle z \rangle \sim 3.6$, (Gruppioni et al. 2013, IR)	No correction
2.49	-4.65 ± 0.14
2.99	-5.75 ± 0.13
3.48	-7.18 ± 0.43
$z \sim 3.8$, (van der Burg et al. 2010, UV)	Dust corrected
0.33	-1.99 ± 0.22
0.47	-2.08 ± 0.08
0.62	-2.13 ± 0.06
0.76	-2.23 ± 0.05
0.91	-2.31 ± 0.07
1.06	-2.47 ± 0.09
1.20	-2.62 ± 0.05
1.35	-2.77 ± 0.04
1.50	-3.02 ± 0.02
1.64	-3.27 ± 0.04
1.79	-3.54 ± 0.02
1.93	-3.93 ± 0.06
2.08	-4.27 ± 0.10
2.23	-4.88 ± 0.05

Table 3. Stepwise SFR functions at $z \sim 3.1$ using the data from Reddy et al. (2008), orange circles in the top right panel of Fig. 1, van der Burg et al. (2010), blue triangles in the top right panel of Fig. 1 and Parsa et al. (2016), grey squares in the top right panel of Fig. 1.

$\log \frac{\mathrm{SFR}}{\mathrm{M}_\odot\ \mathrm{yr}^{-1}}$	$\log \phi_{\mathrm{SFR}}\ (\mathrm{Mpc}^{-3}\ \mathrm{dex}^{-1})$
$z \sim 3.0$, Parsa et al. (2016, UV)	Dust corrected
−1.06	-1.54 ± 0.03
−0.86	-1.51 ± 0.03
−0.66	-1.44 ± 0.03
−0.42	-1.61 ± 0.04
−0.17	-1.60 ± 0.04
0.08	-1.77 ± 0.05
0.33	-1.83 ± 0.05
0.58	-2.06 ± 0.02
0.84	-2.12 ± 0.02
1.09	-2.30 ± 0.02
1.39	-2.53 ± 0.03
1.60	-3.03 ± 0.01
1.84	-3.63 ± 0.03
2.09	-4.34 ± 0.08
2.35	-5.22 ± 0.14
$z \sim 3.1$, van der Burg et al. (2010, UV)	Dust corrected
0.43	-1.97 ± 0.20
0.58	-1.80 ± 0.08
0.73	-1.91 ± 0.10
0.89	-2.03 ± 0.08
1.04	-2.13 ± 0.07
1.19	-2.24 ± 0.09
1.34	-2.40 ± 0.10
1.49	-2.58 ± 0.06
1.64	-2.78 ± 0.05
1.79	-3.07 ± 0.05
1.94	-3.42 ± 0.11
2.09	-3.72 ± 0.15
2.25	-4.13 ± 0.14
2.40	-4.63 ± 0.12
2.55	-5.48 ± 0.43
2.70	-5.48 ± 0.43
$z \sim 3.1$, Reddy et al. (2008, Bolometric)	Dust corrected
−0.14	-1.59 ± 0.27
0.09	-1.69 ± 0.24
0.36	-1.83 ± 0.24
0.61	-2.02 ± 0.27
0.86	-2.22 ± 0.26
1.11	-2.41 ± 0.21
1.36	-2.60 ± 0.18
1.61	-2.83 ± 0.13
1.86	-3.11 ± 0.11
2.11	-3.40 ± 0.08
2.36	-3.73 ± 0.12
2.61	-4.12 ± 0.12

Finally, we use the IR LF of Magnelli et al. (2011) for redshifts $1.8 < z < 2.3$. We convert the IR luminosities to SFRs using equation (3). We obtain the analytic form (red dashed line) converting the analytic LFs to SFRFs following Smit et al. (2012). The results of Magnelli et al. (2011) span the range ∼40–1380 $\mathrm{M}_\odot\ \mathrm{yr}^{-1}$ but we extend the Schechter (1976) form to lower SFRs, so we can have a comparison with the other data sets present in this work. We note that Magnelli et al. (2011) obtained the CSFRD by integrating the extended Schechter (1976) form of their LF (without limits) so they can compare their results with other authors. This methodology was employed by most authors, thus we extend the analytic expressions of the SFRFs to lower SFRs at all panels. The SFRFs for $z \sim 2.2$ galaxies from our analysis are presented in the bottom right panel of Fig. 1 and Table 5. We see an excellent agreement between the different SFRFs derived from various SFR tracers. As we have seen in the previous subsections the results from the IR LF (Magnelli et al. 2011) provide information for high star-forming systems while the bolometric luminosity of Reddy et al. (2008) spans a wider range of SFRs due to their UV data. The SFRF we obtain from the Hα results of Sobral et al. (2013) is in good agreement with the other two.

3.5 The star formation rate function at $z \sim 2.0$

To determine the SFRF of $z \sim 2.0$ galaxies, we use the IR LF from Magnelli et al. (2011, $1.8 < z < 2.3$) and the UV LFs of Alavi et al. (2014, $z \sim 2.0$) and Parsa et al. (2016, $z \sim 2.0$). We use equations (3) and (1) to convert the IR and UV luminosities to

Table 4. Stepwise determinations of the SFR function at $z \sim 2.6$ (red diamonds in Fig. 1) using the IR LF of Gruppioni et al. (2013) for $2.5 < z < 3.0$. The parameters of the analytic expression (dark green dotted line in Fig. 1) we obtain from dust correcting the Schechter (1976) fit given by Oesch et al. (2010) are: $\phi^\star = 0.0026$ Mpc^{-3}, SFR$^\star = 24.56$ M$_\odot$ yr^{-1} and $\alpha = -1.48$.

$\log \frac{\mathrm{SFR}}{\mathrm{M}_\odot\ \mathrm{yr}^{-1}}$	$\log \phi_{\mathrm{SFR}}$ (Mpc^{-3} dex^{-1})
$z \sim 2.5$–3.0, Gruppioni et al. (2013, IR)	No correction
2.49	-3.75 ± 0.21
2.99	-4.15 ± 0.11
3.49	-5.11 ± 0.07

Table 5. Stepwise SFR functions at $z \sim 2.2$ using the data from Reddy et al. (2008), orange circles in the bottom right panel of Fig. 1, Magnelli et al. (2011), red circles in the top bottom right of Fig. 1 and Sobral et al. (2013), blue circles in the bottom right panel of Fig. 1.

$\log \frac{\mathrm{SFR}}{\mathrm{M}_\odot\ \mathrm{yr}^{-1}}$	$\log \phi_{\mathrm{SFR}}$ (Mpc^{-3} dex^{-1})
$z \sim 2.23$, Sobral et al. (2013, Hα)	Dust corrected
0.90	-1.93 ± 0.19
1.05	-2.07 ± 0.16
1.20	-2.19 ± 0.07
1.30	-2.31 ± 0.05
1.40	-2.41 ± 0.05
1.50	-2.50 ± 0.04
1.60	-2.59 ± 0.05
1.70	-2.73 ± 0.06
1.80	-2.88 ± 0.14
1.90	-3.09 ± 0.17
2.00	-3.33 ± 0.22
2.10	-3.67 ± 0.31
2.20	-4.01 ± 0.51
$z \sim 2.3$, Magnelli et al. (2011, IR)	Dust corrected
1.64	-2.72 ± 0.25
1.94	-3.05 ± 0.25
2.24	-3.29 ± 0.25
2.54	$-3.88 \pm^{0.26}_{0.27}$
2.84	$-4.84 \pm^{0.34}_{0.58}$
3.14	$-5.14 \pm^{0.39}_{3.00}$
$z \sim 1.9$–2.7, Reddy et al. (2008, Bolometric)	Dust corrected
-0.14	-1.43 ± 0.21
0.09	-1.49 ± 0.17
0.36	-1.61 ± 0.17
0.61	-1.79 ± 0.22
0.86	-1.98 ± 0.23
1.11	-2.16 ± 0.21
1.36	-2.37 ± 0.19
1.61	-2.60 ± 0.14
1.86	-2.86 ± 0.13
2.11	-3.18 ± 0.09
2.36	-3.51 ± 0.09
2.61	-3.93 ± 0.14

SFRs, respectively. The SFRF resulting from the IR data of Magnelli et al. (2011) suggests that the UV selection of Alavi et al. (2014) and Parsa et al. (2016) misses a significant number of objects at $z \sim 2.0$ or that dust corrections implied by the IRX–β relation and UV SFRs are underestimated at the bright end of the distribution. This is similar with what we saw at redshift $z \sim 2.6$ and Section 3.3. The SFRF that is obtained from the data of Parsa et al. (2016) implies

Table 6. Stepwise SFR functions at $z \sim 2.0$ using the data from Parsa et al. (2016, grey squares of Fig. 2). The parameters of the analytic expression (black dotted line) we obtain from dust correcting the Schechter (1976) fit given by Alavi et al. (2014) are $\phi^\star = 0.0023$ Mpc^{-3}, SFR$^\star = 23.6$ M$_\odot$ yr^{-1} and $\alpha = -1.58$.

$\log \frac{\mathrm{SFR}}{\mathrm{M}_\odot\ \mathrm{yr}^{-1}}$	$\log \phi_{\mathrm{SFR}}$ (Mpc^{-3} dex^{-1})
$z \sim 2.0$, Parsa et al. (2016, UV)	Dust corrected
-1.56	-1.17 ± 0.02
-1.26	-1.22 ± 0.02
-1.06	-1.44 ± 0.03
-0.81	-1.45 ± 0.03
-0.56	-1.54 ± 0.04
-0.30	-1.60 ± 0.04
-0.05	-1.70 ± 0.04
0.20	-1.80 ± 0.05
0.45	-1.89 ± 0.02
0.70	-2.00 ± 0.02
0.95	-2.16 ± 0.02
1.21	-2.48 ± 0.03
1.46	-2.95 ± 0.14
1.71	-3.52 ± 0.27
1.96	-4.17 ± 0.57
2.21	-4.62 ± 0.98

a distribution much shallower at low SFRs than that suggested by Magnelli et al. (2011) and Alavi et al. (2014). The results from the above analysis are shown in Table 6 and Fig. 2.

3.6 The star formation rate function at $z \sim 1.5$

To obtain the SFRF at redshift $z \sim 1.5$, we use the UV LF of Cucciati et al. (2012, $z \sim 1.2$–1.7), the IR LFs from Magnelli et al. (2011, $z \sim 1.3$–1.8) and Gruppioni et al. (2013, $z \sim 1.2$–1.7) and the Hα LF from Sobral et al. (2013, $z \sim 1.47$). The LFs of Magnelli et al. (2011) and Sobral et al. (2013) provide information about the intermediate and high star-forming objects. The SFRFs from the IR LFs imply that the dust corrections used to recover the Hα LF of Sobral et al. (2013) were underestimated for high star-forming systems or that the Hα selection of the authors misses a significant number of dusty objects. As discussed in Section 2.2, the 1 mag simplification that is commonly used for dust attenuation effects underestimates the intrinsic SFRs for $z > 0.3$. Maybe this is the reason of the inconsistency between the two SFRFs. The SFRF we obtain from the analytic UV LF of Cucciati et al. (2012) provides information at low SFRs and implies a shallower distribution. The results are in perfect agreement with the SFRF obtained from Sobral et al. (2013) for high SFRs. Thus, the IRX–β relation may also underestimate the true SFR of high star-forming objects. The characteristic SFR[2] implied by UV and Hα data is much lower than that of IR studies. The SFRFs for $z \sim 1.5$ from the above analysis are shown in the top right panel of Fig. 2 and Table 7.

3.7 The star formation rate function at $z \sim 1.15$

To obtain an estimate of the SFRF at redshift $z \sim 1.15$, we use the IR LFs from Gruppioni et al. (2013, $z \sim 1.0$–1.2) and

[2] The characteristic luminosity of an LF is the luminosity at which the power-law form becomes an exponential choke. We define the characteristic SFR as the SFR at which the behaviour of the SFRF changes from an exponential to a power law.

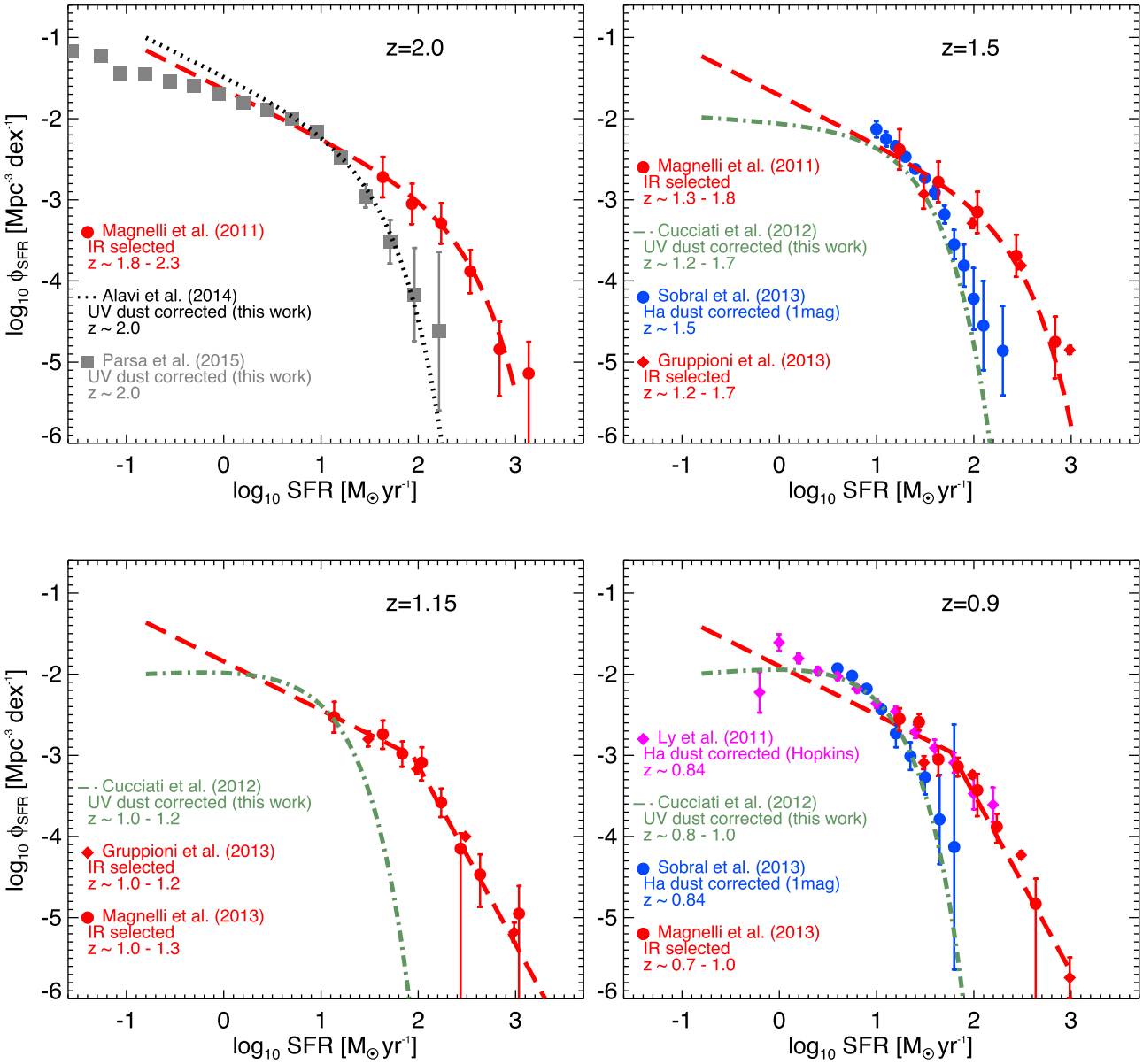

Figure 2. The stepwise and analytical determinations of the observed SFRF for redshifts $z \sim 2.0$ (top left panel), $z \sim 1.5$ (top right panel), $z \sim 1.15$ (bottom left panel) and $z \sim 0.9$ (bottom right panel). The blue filled circles are the SFRFs for $z \sim 0.9$ and $z \sim 1.5$ estimated using the Hα LF from Sobral et al. (2013). The red filled circles and red dashed lines are obtained using the IR LF from Magnelli et al. (2011) and Magnelli et al. (2013). The dark green dash–dotted lines are the analytic Schechter (1976) fits that we obtain after dust correcting the UV LF of Cucciati et al. (2012). The red filled diamonds are the SFRFs for redshifts $z \sim 0.9$, $z \sim 1.15$ and $z \sim 1.5$ using the IR LFs from Gruppioni et al. (2013). The magenta filled diamonds are the stepwise determination of the SFRF for $z \sim 0.9$ using the Hα LF from Ly et al. (2011). The dotted black line is the analytic SFRF that we obtained using the UV LF from Alavi et al. (2014, $z \sim 1.9$). For the grey squares, we used the UV LF from Parsa et al. (2016, $z \sim 2$).

Magnelli et al. (2013, $z \sim$ 1.0–1.3) and the FUV LF of Cucciati et al. (2012, $z \sim$ 1.0–1.2). Even at these intermediate redshifts, the IR surveys are unable to probe low star-forming objects. The red dashed line is the analytical SFRF obtained from the double power-law fit of the LF of Magnelli et al. (2013). The results from the FUV LF of Cucciati et al. (2012) imply a much shallower SFRF with a much lower characteristic SFR. Once again we see that the SFRFs from the extrapolations of IR studies typically have higher characteristic SFRs and are steeper for faint objects than those found by UV data. Our results for the SFRF at redshift $z \sim 1.15$ are in the bottom left panel of Fig. 2 and Table 8.

3.8 The star formation rate function at $z \sim 0.9$

To retrieve the SFRF at redshift $z \sim 0.9$, we use the LFs of Ly et al. (2011, $z \sim 0.84$), Gruppioni et al. (2013, ~0.8–1.0), Cucciati et al. (2012, ~0.8–1.0), Magnelli et al. (2013, $z \sim$ 0.7–1.0) and Sobral et al. (2013, $z \sim 0.84$). As discussed in Section 2.2, the LF of Ly et al. (2011) is an Hα LF that is corrected for incompleteness and dust attenuation effects with the Hopkins et al. (2001) dust correction law. This dust correction law implies a luminosity/SFR dependent correction with the observed (non-intrinsic) luminosity/SFR. To obtain the SFRF from this Hα LF we use equation (2). The magenta filled diamonds of Fig. 2 are the stepwise determination of the SFRF

Table 7. Stepwise SFR functions at $z \sim 1.5$ using the data from Sobral et al. (2013), blue circles of Fig. 2 and Magnelli et al. (2011), red circles of Fig. 2. The parameters of the analytic expression (dark green dot–dashed line) we obtain from dust correcting the Schechter (1976) fit given by Cucciati et al. (2012) are $\phi^\star = 0.0033$ Mpc^{-3}, SFR$^\star = 16.7$ M$_\odot$ yr^{-1} and $\alpha = -1.07$.

$\log \frac{\mathrm{SFR}}{\mathrm{M}_\odot\ \mathrm{yr}^{-1}}$	$\log \phi_{\mathrm{SFR}}$ (Mpc^{-3} dex^{-1})
$z \sim 1.47$, Sobral et al. (2013, Hα)	1 Mag, incompleteness checked
1.00	-2.13 ± 0.10
1.10	-2.25 ± 0.09
1.20	-2.34 ± 0.06
1.30	-2.47 ± 0.05
1.40	-2.62 ± 0.05
1.50	-2.73 ± 0.04
1.60	-2.91 ± 0.08
1.70	-3.18 ± 0.11
1.80	-3.55 ± 0.18
1.90	-3.81 ± 0.26
2.00	-4.22 ± 0.38
2.10	-4.55 ± 0.55
2.30	-4.86 ± 0.55
$z \sim 1.3$–1.8, Magnelli et al. (2011, IR)	No correction
1.24	-2.38 ± 0.25
1.64	-2.78 ± 0.25
2.04	$-3.15^{+0.25}_{-0.26}$
2.44	-3.69 ± 0.26
2.84	$-4.75^{+0.31}_{-0.45}$
$z \sim 1.2$–1.7, Gruppioni et al. (2013, IR)	No correction
1.49	-2.93 ± 0.18
1.99	-3.29 ± 0.06
2.49	-3.81 ± 0.03
2.99	-4.85 ± 0.05

Table 8. Stepwise SFR functions at $z \sim 1.15$ using the data from Gruppioni et al. (2013, red diamonds of Fig. 2) and Magnelli et al. (2013, red circles in the bottom left panel of Fig. 2). The parameters of the analytic expression (dark green dot–dashed line) we obtain from dust correcting the Schechter (1976) fit given by Cucciati et al. (2012) are $\phi^\star = 0.006$ Mpc^{-3}, SFR$^\star = 8.3$ M$_\odot$ yr^{-1} and $\alpha = -0.93$.

$\log \frac{\mathrm{SFR}}{\mathrm{M}_\odot\ \mathrm{yr}^{-1}}$	$\log \phi_{\mathrm{SFR}}$ (Mpc^{-3} dex^{-1})
$z \sim 1.0$–1.2, Gruppioni et al. (2013, IR selected)	No correction
1.49	-2.80 ± 0.09
1.99	-3.17 ± 0.06
2.49	-4.00 ± 0.03
2.99	-5.18 ± 0.12
$z \sim 1.0$–1.3, Magnelli et al. (2013, IR selected)	No correction
1.14	-2.53 ± 0.19
1.64	$-2.74^{+0.17}_{-0.18}$
1.84	$-2.98^{+0.15}_{-0.16}$
2.04	$-3.09^{+0.19}_{-0.22}$
2.24	$-3.58^{+0.17}_{-0.18}$
2.44	$-4.15^{+0.19}_{-4.15}$
2.64	$-4.47^{+0.25}_{-0.40}$
3.04	$-4.95^{+0.34}_{-4.95}$

for $z \sim 0.84$ from the Hα LF of Ly et al. (2011). From Fig. 2, we see that the bright end of the SFRF from Ly et al. (2011) is in excellent agreement with the results from the IR samples and this suggests that the SFR dependent dust corrections suggested by Hopkins et al. (2001) are robust. For the low star-forming objects, we see that the SFRFs derived from Ly et al. (2011) and Sobral et al. (2013) are in very good agreement. However, the SFRFs that rely on the results of Sobral et al. (2013) are highly uncertain for luminous star-forming objects and is not consistent with the SFRs of the IR samples. Sobral et al. (2013) made a direct comparison between their Hα LF and that of Ly et al. (2011) assuming the same dust correction law for both samples. The two LFs are in excellent agreement. This indicates that the 1 mag simplification is responsible for the tension with the IR SFRs and is not valid at $z \sim 0.9$, since it underestimates the intrinsic SFRs/luminosities. Generally the 1mag correction is expected to overestimate the SFR for low-mass (low dust contents) objects and underestimates it for high-mass (high dust contents) objects, thus the SFRF from the results of Sobral et al. (2013) could be artificially steep. The results for the SFRF at $z \sim 0.9$ from the above analysis are shown in the bottom right panel of Fig. 2 and Table 9.

In conclusion, SFRFs that rely on UV data are shallower than those obtained from IR LFs. The latter are unable to probe objects with low SFR and thus their extrapolation, which is commonly used to calculate the CSFRD, includes a lot of uncertainties. On the other hand, UV SFRFs–LFs are unable to successfully probe high SFR systems due to the fact that they either fail to take into account dusty and massive objects or dust correction laws underestimate dust corrections, and hence intrinsic SFRs, in this range. Despite the differences at the faint and bright ends of the distribution, UV, Hα and IR SFR indicators show excellent agreement for objects with $-0.3 \leq \log(\mathrm{SFR}/(\mathrm{M}_\odot\ \mathrm{yr}^{-1})) \leq 1.5$.

4 SIMULATIONS

In this work, we use the set of ANGUS described in Tescari et al. (2014).[3] We run these simulations using the hydrodynamic code P-GADGET3(XXL). We assume a flat Λ cold dark matter model with $\Omega_{0\mathrm{m}} = 0.272$, $\Omega_{0\mathrm{b}} = 0.0456$, $\Omega_\Lambda = 0.728$, $n_\mathrm{s} = 0.963$, $H_0 = 70.4$ km s^{-1} Mpc^{-1} (i.e. $h = 0.704$) and $\sigma_8 = 0.809$. Our configurations have box size $L = 24$ Mpc h^{-1}, initial mass of the gas particles $M_\mathrm{GAS} = 7.32 \times 10^6$ M$_\odot$ h^{-1} and a total number of particles equal to 2×288^3. All the simulations start at $z = 60$ and were stopped at $z = 0.8$. The different configurations were constrained at $z \sim 4$–7 using the observations of Smit et al. (2012) in Tescari et al. (2014).

We explore different feedback prescriptions, in order to understand the origin of the difference between observed and simulated relationships. We do not explore the broadest possible range of simulations, but concentrate on the simulations that can describe the high-z SFRF and GSMF (Tescari et al. 2014; Katsianis et al. 2015). We performed resolution tests for high redshifts ($z \sim 4$–7) in the appendix of Katsianis et al. (2015) and showed that our results converge for objects with $\log_{10}(M_\star/\mathrm{M}_\odot) \geq 8.5$.

4.1 SNe feedback

We investigate the effect of three different galactic winds schemes in the simulated SFRF. First, we use the implementation of the constant galactic winds (Springel & Hernquist 2003). We assume the wind

[3] The features of our code are extensively described in Tescari et al. (2014) and Katsianis et al. (2015), therefore we refer the reader to those papers for additional information.

Table 9. Stepwise SFR functions at $z \sim 0.9$ using the data from Ly et al. (2011), magenta diamonds of Fig. 2, Gruppioni et al. (2013), red diamonds in the bottom right of Fig. 2, Magnelli et al. (2013), red circles of Fig. 2 and Sobral et al. (2013), blue circles of Fig. 2. The parameters of the analytic expression (dark green dot–dashed line) we obtain from dust correcting the Schechter (1976) fit given by Cucciati et al. (2012) are $\phi^\star = 0.007$ Mpc^{-3}, SFR$^\star = 7.75$ M$_\odot$ yr^{-1} and $\alpha = -0.88$.

$\log \frac{\mathrm{SFR}}{\mathrm{M}_\odot\ \mathrm{yr}^{-1}}$	$\log \phi_{\mathrm{SFR}}$ (Mpc^{-3} dex^{-1})
$z \sim 0.84$, Sobral et al. (2013, Hα selected)	1 mag, incompleteness checked
0.60	-1.93 ± 0.03
0.75	-2.02 ± 0.03
0.90	-2.18 ± 0.04
1.05	-2.43 ± 0.06
1.20	-2.73 ± 0.17
1.35	-3.01 ± 0.17
1.50	-3.27 ± 0.21
1.65	-3.79 ± 0.55
1.80	-4.13 ± 1.51
$z \sim 0.8$–1.0, Magnelli et al. (2013, IR selected)	No correction
1.49	-3.09 ± 0.08
1.99	-3.24 ± 0.04
2.49	-4.23 ± 0.05
2.99	-5.74 ± 0.25
$z \sim 0.7$–1.0, Gruppioni et al. (2013, IR selected)	No correction
1.24	$-2.55^{+0.13}_{-0.15}$
1.44	$-2.59^{+0.10}_{-0.10}$
1.64	$-3.05^{+0.16}_{-0.20}$
1.84	$-3.14^{+0.11}_{-0.12}$
2.04	$-3.43^{+0.20}_{-0.32}$
2.24	$-3.88^{+0.16}_{-0.20}$
2.64	$-4.83^{+0.31}_{-4.83}$
$z \sim 0.84$, Ly et al. (2011, Hα selected)	Dust corrected, incompleteness checked
−0.20	-2.22 ± 0.25
−0.002	-1.61 ± 0.10
0.20	-1.81 ± 0.06
0.40	-1.96 ± 0.05
0.60	-2.03 ± 0.04
0.80	-2.18 ± 0.05
1.00	-2.36 ± 0.05
1.20	-2.46 ± 0.06
1.40	-2.71 ± 0.08
1.60	-2.91 ± 0.10
1.80	-3.09 ± 0.12
2.00	-3.47 ± 0.19
2.19	-3.61 ± 0.21

mass loading factor $\eta = \dot{M}_\mathrm{w}/\dot{M}_\star = 2$ and a fixed wind velocity $v_\mathrm{w} = 450$ km s^{-1}. Puchwein & Springel (2013) demonstrated that constant wind models are not able to reproduce the observed GSMF at $z \sim 0$. Thus, similar to the authors, we explore as well the effects of variable wind models, in which the wind velocity is proportional to the escape velocity of the galaxy from which the wind is launched. This choice is supported by the observations of Martin (2005) who detect a positive correlation of galactic outflow speed with galaxy mass and showed that the outflow velocities are always two to three times larger than the galactic rotation speed. Inspired by these results, Puchwein & Springel (2013) and Barai et al. (2013) assume that the velocity v_max is related to the circular velocity v_circ. We use a momentum-driven wind model in which the velocity of the winds is proportional to the circular velocity v_circ of the galaxy:

$$v_\mathrm{w} = 2\sqrt{\frac{G\mathrm{M}_\mathrm{halo}}{R_{200}}} = 2 \times v_\mathrm{circ}, \tag{7}$$

and the loading factor η,

$$\eta = 2 \times \frac{450\ \mathrm{km\,s^{-1}}}{v_\mathrm{w}}, \tag{8}$$

where M_halo is the halo mass and R_{200} is the radius within which a density 200 times the mean density of the Universe at redshift z is enclosed (Barai et al. 2013). Furthermore, we investigate the effect of the energy-driven winds used by Puchwein & Springel (2013). In this case the loading factor is

$$\eta = 2 \times \left(\frac{450\ \mathrm{km\,s^{-1}}}{v_\mathrm{w}}\right)^2, \tag{9}$$

while $v_\mathrm{w} = 2 \times v_\mathrm{circ}$.

4.2 AGN feedback

In our scheme for AGN feedback, when a dark matter halo reaches a mass above a given mass threshold $M_\mathrm{th} = 2.9 \times 10^{10}$ M$_\odot\,h^{-1}$ for the first time, it is seeded with a central supermassive black hole (SMBH) of mass $M_\mathrm{seed} = 5.8 \times 10^4$ M$_\odot\,h^{-1}$ (provided it contains a minimum mass fraction in stars $f_\star = 2.0 \times 10^{-4}$). Each SMBH will then increase its mass through mergers or by accreting local gas from a maximum accretion radius $R_\mathrm{ac} = 200$ kpc h^{-1}. In Tescari et al. (2014), we labelled the above feedback prescription as the early AGN feedback recipe. In this scheme, we allow the presence of black hole seeds in relatively low-mass haloes ($M_\mathrm{th} \leq 2.9 \times 10^{10}$ M$_\odot\,h^{-1}$). Thus, SMBHs start to occupy dark matter haloes at high redshifts and have enough time to grow and produce efficient feedback at $z \leq 2$. The AGN feedback prescription that we use combined with efficient winds is successful at reproducing the observed SFRF (Tescari et al. 2014) and GSMF (Katsianis et al. 2015) for redshifts $4 < z < 7$.

5 THE STAR FORMATION RATE FUNCTION IN HYDRODYNAMIC SIMULATIONS

In Fig. 3, we present the evolution of the SFRF from redshift $z \sim 4.0$ to $z \sim 2.2$ for our different runs and compare these with the observations discussed in Section 3. Like in Tescari et al. (2014), we name each run according to the IMF, boxsize and combination of feedback prescriptions that were used (more details can be found in Table 10). At each redshift, a panel showing ratios between the different simulations and the *Kr24_eA_sW* run (red dot–dashed line) is included. The *Kr24_eA_sW* run was the reference model used in Tescari et al. (2014, SFRF, $z \sim 4$–7) and Katsianis et al. (2015, GSMF, $z \sim 4$–7). The constant wind model was used to model galactic winds in this case. This run produces similar results of simulations with variable galactic winds (energy-driven winds – EDW and momentum-driven winds – MDW) at high redshift and we will use it as a reference in the following comparisons, despite the fact that it is not as successful at $z \sim 1$–4.

At redshift $z = 3.8$ (top left panel of Fig. 3), we see that the *Ch24_NF* run (no feedback, magenta triple dot–dashed line) overproduces the number of systems with respect to all the other

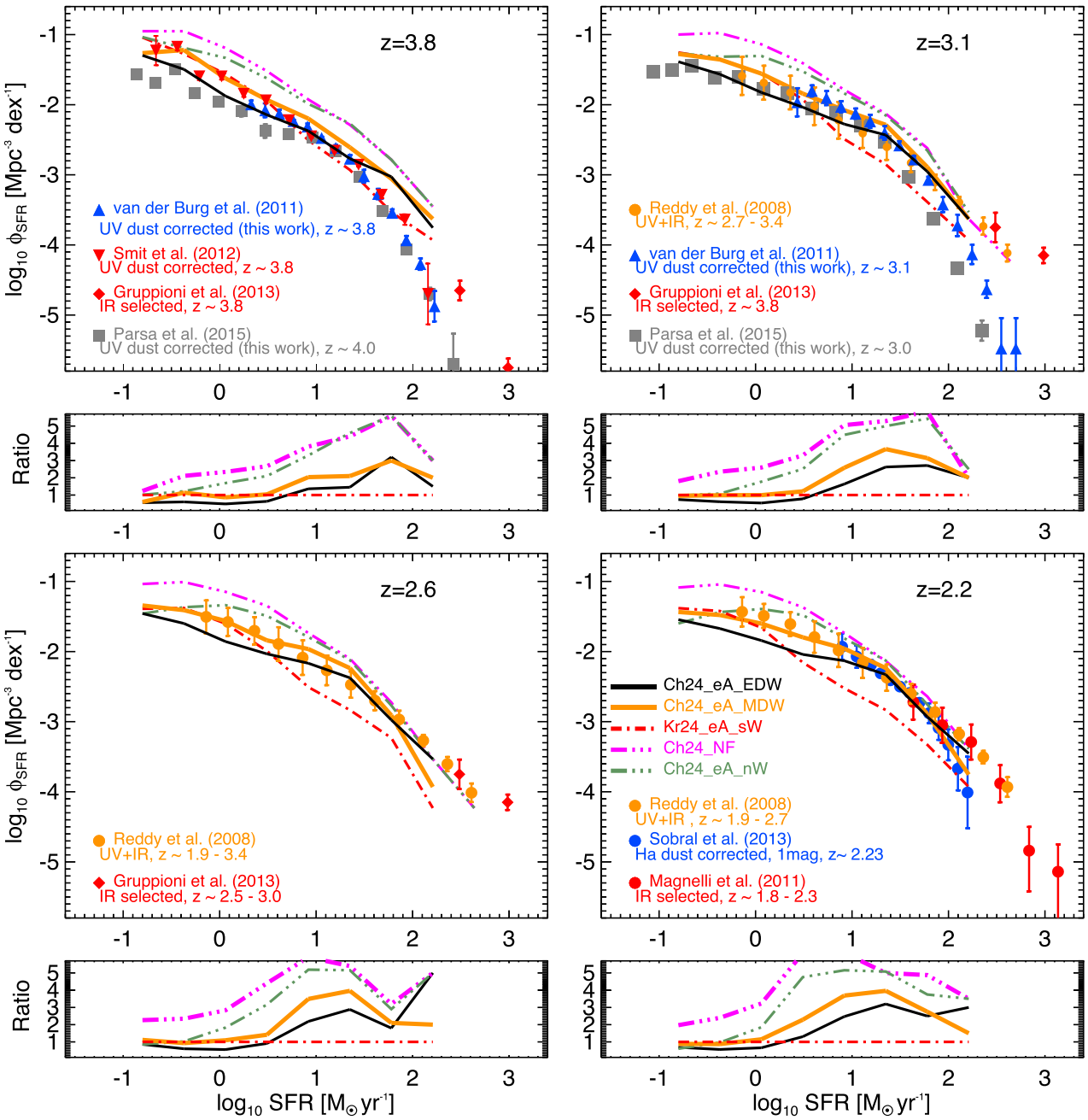

Figure 3. The simulated SFRFs (lines) for redshifts $z \sim 3.8$ (top left panel), $z \sim 3.1$ (top right panel), $z \sim 2.6$ (bottom left panel) and $z \sim 2.2$ (bottom right panel). Alongside we present the stepwise determinations of the observed SFRFs of Fig. 1 for comparison.

simulations and observations, due to the overcooling of gas. Tescari et al. (2014) discussed the effect of our feedback implementations on the simulated SFRF for redshifts $4 < z < 7$ and suggested that some form of feedback is necessary. As discussed in Tescari et al. (2014), the *Kr24_eA_sW* and *Ch24_eA_MDW* runs show a good consistency with observations from UV-selected samples (e.g. Smit et al. 2012). Variations to the IMF have a negligible impact on our simulated galaxy SFRF. The *Ch24_eA_MDW* run slightly overproduces high star-forming objects since winds are less effective in this wind model for high-mass/SFR systems. The *Ch24_eA_EDW* run shows a good agreement with observations but underpredicts the number of objects with low SFRs with respect to other runs. This is due to the fact that the winds of this model are very effective for low-mass/SFR systems. We see that all the models implemented with galactic winds are able to broadly reproduce the observations, indicating that their presence is important.

We note a similar trend at redshift $z = 3.1$ (top right panel of Fig. 3). The runs without winds overpredict the number of objects at all SFRs. We see that the *Kr24_eA_sW* run starts to underpredict objects with $\log(\mathrm{SFR}/(\mathrm{M}_\odot\,\mathrm{yr}^{-1})) \geq 0.5$ with respect the *Ch24_eA_MDW* and *Ch24_eA_EDW* runs. The last two have better consistency with observations. The *Ch24_eA_MDW* and *Ch24_eA_EDW* runs produce almost identical SFRFs for objects with $\log(\mathrm{SFR}/(\mathrm{M}_\odot\,\mathrm{yr}^{-1})) \geq 0.5$, but the second produces less objects with $\log(\mathrm{SFR}/(\mathrm{M}_\odot\,\mathrm{yr}^{-1})) \leq 0.5$ due to the fact that energy variable driven winds are more effective in this range. This

Table 10. Summary of the different runs used in this work. Column 1, run name; column 2, IMF chosen; column 3, box size in comoving Mpc h^{-1}; column 4, total number of particles ($N_{\rm TOT} = N_{\rm GAS} + N_{\rm DM}$); column 5, mass of the dark matter particles; column 6, initial mass of the gas particles; column 7, Plummer-equivalent comoving gravitational softening length; column 8, type of feedback implemented. See Section 4 and Tescari et al. (2014) for more details on the parameters used for the different feedback recipes.

Run	IMF	Box size (Mpc h^{-1})	$N_{\rm TOT}$	$M_{\rm DM}$ ($M_\odot\ h^{-1}$)	$M_{\rm GAS}$ ($M_\odot\ h^{-1}$)	Comoving softening (kpc h^{-1})	Feedback
Kr24_eA_sW	Kroupa	24	2×288^3	3.64×10^7	7.32×10^6	4.0	Early AGN + Constant strong winds
Ch24_eA_nW	Chabrier	24	2×288^3	3.64×10^7	7.32×10^6	4.0	Early AGN + no winds
Ch24_NF	Chabrier	24	2×288^3	3.64×10^7	7.32×10^6	4.0	No feedback
Ch24_eA_MDW[a]	Chabrier	24	2×288^3	3.64×10^7	7.32×10^6	4.0	Early AGN + Momentum-driven winds
Ch24_eA_EDW[b]	Chabrier	24	2×288^3	3.64×10^7	7.32×10^6	4.0	Early AGN + Energy-driven winds

[a] In this simulation, we adopt variable momentum-driven galactic winds (Section 4.1).
[b] In this simulation, we adopt variable energy-driven galactic winds (Section 4.1).

brings simulations into better agreement with the data of Parsa et al. (2016).

At redshift $z = 2.6$ (bottom left panel of Fig. 3), we see once again that the simulation with constant energy-driven winds tend to underpredict objects with high SFRs. There is no need to strongly quench the SFR of high star-forming objects and all the configurations, including the *Ch24_NF* run, are consistent with the observations for objects with $\log(\mathrm{SFR}/(\mathrm{M}_\odot\ \mathrm{yr}^{-1})) \geq 1.5$. It is necessary though to have a feedback prescription to decrease the SFRs of objects with $\log(\mathrm{SFR}/(\mathrm{M}_\odot\ \mathrm{yr}^{-1})) \leq 1.5$. The efficient variable momentum and energy-driven winds are good candidates. The *Ch24_eA_MDW* and *Ch24_eA_EDW* runs are consistent with the observations, even though the *Ch24_eA_EDW* run slightly underpredicts the number of objects with low SFRs.

At redshift $z = 2.2$ (bottom right panel of Fig. 3), we can see the effect of different feedback prescriptions more clearly. This era represents the peak of the CSFRD, and so it is anticipated that feedback related to stars and SNe will play an important role in the regulation of star formation. Constant winds are very efficient for objects with high SFRs and these are common at this epoch. Interestingly, we note that all simulations except *Kr24_eA_sW* and *Ch24_NF* are broadly consistent with observations at $z = 2.2$, but there is a requirement to decrease the number of objects with low SFRs. The *Ch24_eA_nW* and *Ch24_eA_MDW* runs are consistent with the observations, even though the *Ch24_eA_EDW* run slightly underpredicts the number of objects with $\log(\mathrm{SFR}/(\mathrm{M}_\odot\ \mathrm{yr}^{-1})) \leq 0.3$. Despite this, in the following paragraphs we will see that this run is the most successful at lower redshifts because it is able to reproduce the shallow SFRFs obtained from UV LFs.

At redshift $z = 2.0$ (top left panel of Fig. 4), we find that simulations with variable winds are quite successful at reproducing the SFRF implied by the UV LF of Parsa et al. (2016). The *Kr24_eA_sW* run underpredicts objects with high SFR ($\log(\mathrm{SFR}/(\mathrm{M}_\odot\ \mathrm{yr}^{-1})) \geq 0.5$), with respect to all other runs. The run without feedback *Ch24_NF* overpredicts the number of objects with low SFRs, but has good agreement with the constraints from IR studies. This indicates that at $z \sim 2.0$ there is no need for feedback to regulate the SFR of high SFR objects in our simulations. However, efficient feedback is necessary to decrease the number of objects with low SFR, and variable energy-driven winds are perfect candidates.

At redshift $z = 1.5$ (top right panel of Fig. 4) and $z = 1.15$ (bottom left panel of Fig. 4), we see that feedback prescriptions with variable galactic winds are quite successful at reproducing the SFRF implied by the IR LFs, while the *Kr24_eA_sW* run underpredicts objects with high and intermediate star formation. On the other hand, the *Ch24_eA_EDW* and *Ch24_eA_MDW* runs are once again able to reproduce the observations. This is also true for redshift $z = 0.9$ (bottom right panel of Fig. 4). We see that the run without feedback, *Ch24_NF*, overpredicts the number of objects with low SFR but the difference with observations and the rest of the runs is much smaller than at higher redshifts. This could imply the following.

(A) It is possible that galaxies in the *Ch24_NF* run depleted their gas at high redshifts, where the SFRs of the objects were very high at early times. The SFRF in the no feedback scenario at $z \sim 4$ is almost seven times larger than the observations. This could explain the small difference between the SFRFs of the *Ch24_NF* and *Ch24_eA_EDW* configurations at low redshifts, especially at high star-forming objects.

(B) To reproduce the observed evolution of the SFRF we need efficient feedback at early times, while at lower redshifts we require the scheme to become relatively moderate. The *Ch24_eA_EDW* and *Ch24_eA_MDW* runs are successful at reproducing the observations. We saw in Section 4 that variable galactic winds are successful at decreasing the SFRs of objects which reside low-mass haloes. Galaxies reside typically in low mass in the early Universe, so overall this feedback prescription is quite efficient at high redshifts. On the contrary, the scheme becomes relatively moderate at decreasing the SFRs of objects at lower redshifts where haloes have become larger.

In conclusion, the simulation that does not take into account any form of feedback is consistent with the observed SFRF at low and intermediate redshifts, despite the fact that it is in tension with observables at $z > 2.0$. This is a strong indication that the efficiency of feedback prescriptions in our simulations should decrease with time. By construction variable galactic winds are efficient at decreasing the SFR of objects with low mass. Overall this prescription should be more efficient at high redshifts where haloes are typically smaller. On the other hand, at low redshifts haloes are typically larger and this results in winds that become less efficient. This behaviour makes the variable winds a good choice to model galactic outflows in our simulations.

5.1 Best fiducial model

In Figs 5 and 6, we see that the configuration that has the best agreement with observations for all the redshifts considered in this work is the *Ch24_eA_EDW* run, which combines a Chabrier IMF, early AGN feedback and energy-driven winds. In Fig. 5, we show SFRFs at redshift $z \sim 2.2$–4 for our fiducial model (open black diamonds with error bars), alongside the stepwise and analytical

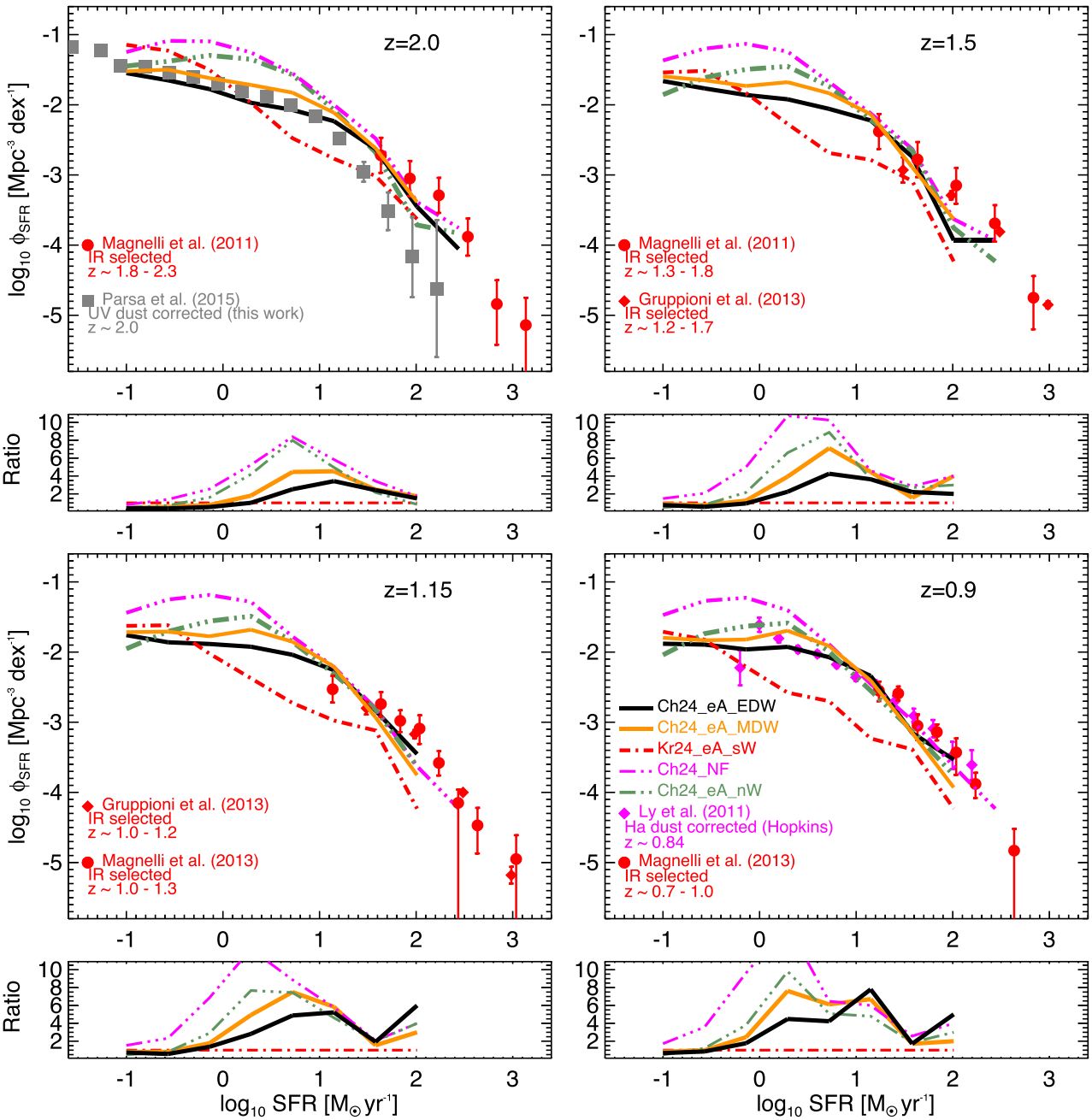

Figure 4. The simulated SFRFs (lines) for redshifts $z \sim 2.0$ (top left panel), $z \sim 1.5$ (top right panel), $z \sim 1.15$ (bottom left panel) and $z \sim 0.9$ (bottom right panel). We also present the stepwise determinations of the observed SFRFs of Fig. 2 for comparison.

determinations of the observed SFRF already presented in Fig. 1. We include Poissonian uncertainties for the simulated SFRFs (black error bars), in order to provide an estimate of the errors from our finite box size. We see that this model is able to reproduce the SFRFs derived from the IR, UV and Hα studies. For low-luminosity/star-forming objects the fiducial run is able to obtain the shallow SFRFs of faint objects implied by UV data, while also being in agreement with the constraints from IR studies for high-luminosity/star-forming systems. Moving to lower redshifts (Fig. 6), we can see a great consistency of the fiducial model with the observations presented in Fig. 2. The simulated SFRFs are in good agreement with the UV and Hα studies for objects with $-1.0 \leq \log(\mathrm{SFR}/(\mathrm{M}_{\odot}\,\mathrm{yr}^{-1})) \leq 1.0$, and with IR data for $\log(\mathrm{SFR}/(\mathrm{M}_{\odot}\,\mathrm{yr}^{-1})) \geq 1.0$. The variable energy-driven winds that efficiently decrease the SFR of low-mass objects are quite successful at reproducing the shallow SFRFs implied by UV data, and also have good agreement with the constraints from IR studies for the high star-forming and dusty objects.

6 THE SIMULATED AND OBSERVED COSMIC STAR FORMATION RATE DENSITY

The evolution of the CSFRD of the Universe is commonly used to test theoretical models, since it represents a fundamental constraint on the growth of stellar mass in galaxies over time. In the above sections, we saw that the SFRFs can commonly be described by the

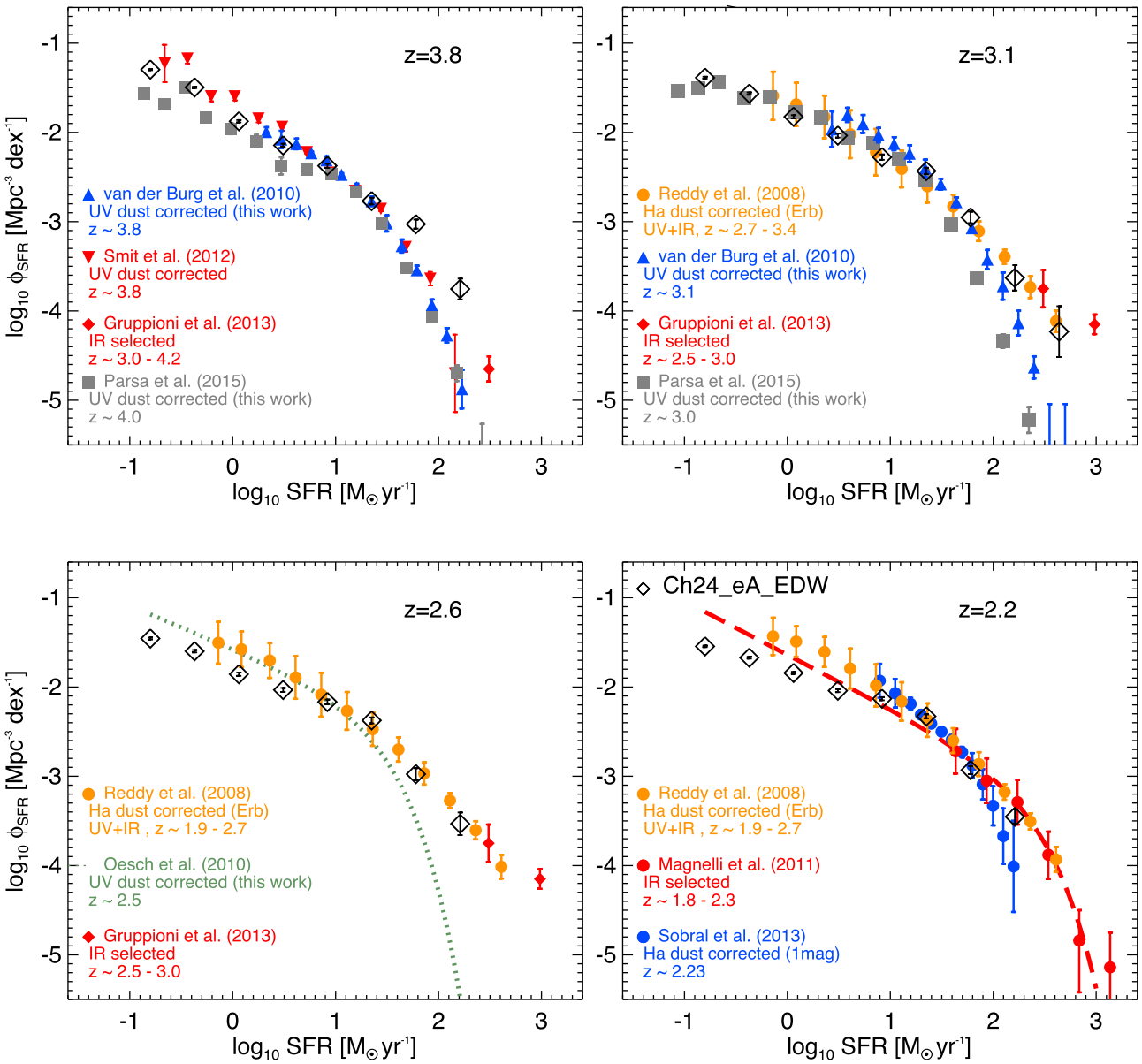

Figure 5. The stepwise and analytical determinations of the observed SFRF along with our fiducial model for redshifts $z \sim 3.8$ (top left panel), $z \sim 3.1$ (top right panel), $z \sim 2.6$ (bottom left panel) and $z \sim 2.2$ (bottom right panel).

Schechter (1976) functional form. The integration of the Schechter (1976) fit gives the total CSFRD of the Universe at a given redshift. It is usual for observers to set limits on to the integration of the LFs when calculating the cosmic luminosity density (LD) that is then converted to CSFRD. Usually, the assumed lower cut corresponds to the sensitivity of the observations available. Madau & Dickinson (2014) used a compilation of LFs to constrain the evolution of CSFRD. The integration limit that the authors chose was $L_{\rm min} = 0.03\,L^{\star}$, where $L^{\star}$ is the characteristic luminosity. The above integration can be written as

$$p_{\rm LD} = \int_{0.03\,L^{\star}}^{\infty} L\,\phi(L,z)\,{\rm d}L, \tag{10}$$

and the integration gives

$$p_{\rm LD} = \Gamma(2+\alpha,\,0.03)\,\phi^{\star}\,L^{\star}, \tag{11}$$

where α is the faint-end slope, which describes how steep the LF is. From equation (11), we see that higher values of characteristic luminosity $L^{\star}$ and faint-end slope α result in higher values of LD (i.e. shallower LFs with small characteristic luminosities give lower LD). After the cosmic LD is calculated, the Kennicutt (1998a) relation can be employed to convert the LD to SFR density. We use the same method and lower limits to integrate the SFRFs presented in Section 3. We also include the $z \sim 4$–8 observations of Bouwens et al. (2012, 2015) and the $z \sim 0$–0.7 observations of Cucciati et al. (2012), Magnelli et al. (2013) and Gruppioni et al. (2013). We present the results in Fig. 7. The results originating from UV observations are in blue, the Hα in green and the IR in red. Reddy et al. (2008) CSFRD originate from a bolometric (UV+IR) luminosity and is in orange. The black dotted line represents the compilation study of Madau & Dickinson (2014).

In the previous sections, we saw that the majority of the SFRFs that we obtained from dust-corrected UV and Hα LFs are

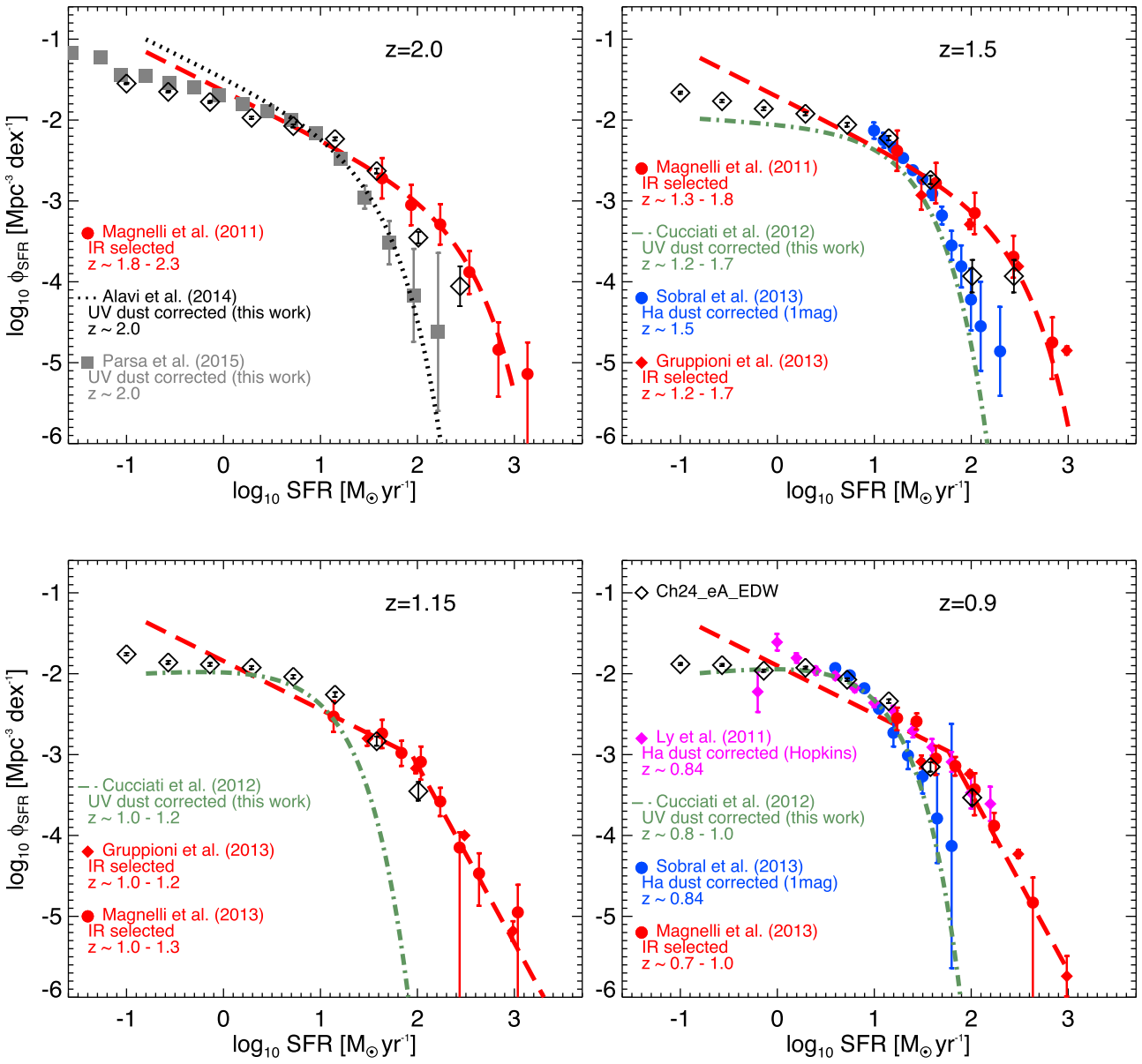

Figure 6. The stepwise and analytical determinations of the SFRF alongside with our best fiducial model for redshifts $z \sim 2.0$ (top left panel), $z \sim 1.5$ (top right panel), $z \sim 1.15$ (bottom left panel) and $z \sim 0.9$ (bottom right panel).

shallower than those from the IR LFs for faint objects. The faint-end slope of the IR SFRF and LF is not directly constrained by individually detected sources and relies on extrapolations. In addition, we demonstrated that IR LFs can more successfully probe dusty, high star-forming objects and therefore the SFRFs they produce, have higher characteristic SFRs than UV and Hα data. These two factors can lead to overestimations in the calculations of the CSFRD that rely solely on IR data.

In agreement with previous work in the literature (Madau & Dickinson 2014), we find that different SFR indicators produce consistent results for the CSFRD and this occurs despite differences in the measurements at the faint and bright end of the SFRF. This is most likely due to the fact that all SFR tracers agree quite well for objects with $-0.3 \leq \log(\mathrm{SFR}/(\mathrm{M}_{\odot}\,\mathrm{yr}^{-1})) \leq 1.5$ (close to the characteristic SFR), which dominate the CSFRD at $z \sim 1$–4. However, the results from IR SFRFs and LFs are typically 0.10–0.25 dex larger. We find that systematics between different SFR indicators do not significantly affect the measurements of the CSFRD despite their differences for low (IR) and high star-forming systems (UV, Hα).

In Fig. 7, we present as well the evolution of the simulated CSFRD for our simulations alongside with the observational constraints. The lower limit of the SFR cut for the simulations has been chosen to match the lower limit assumed in the observations. The simulation with no feedback (*Ch24_NF*) overproduces the CSFRD at all redshifts considered and the peak of star formation activity is at $z \sim 2.5$. At $z \sim 1$–2.5, the CSFRD decreases slowly with time, while at $z \sim 0$–1 the decrement is much faster. This maybe suggests that gas reservoirs were consumed at $z \sim 2$, when the SFR was high and no gas was left to fuel star formation at lower redshifts. If we take into account AGN feedback (*Ch24_eA_nW*), we can see that the simulated CSFRD has a peak once again at $z \sim 2.5$, but starts to decrease and becomes consistent with the observations for $z \sim 0$–1. However, at $z \geq 1.5$ feedback from

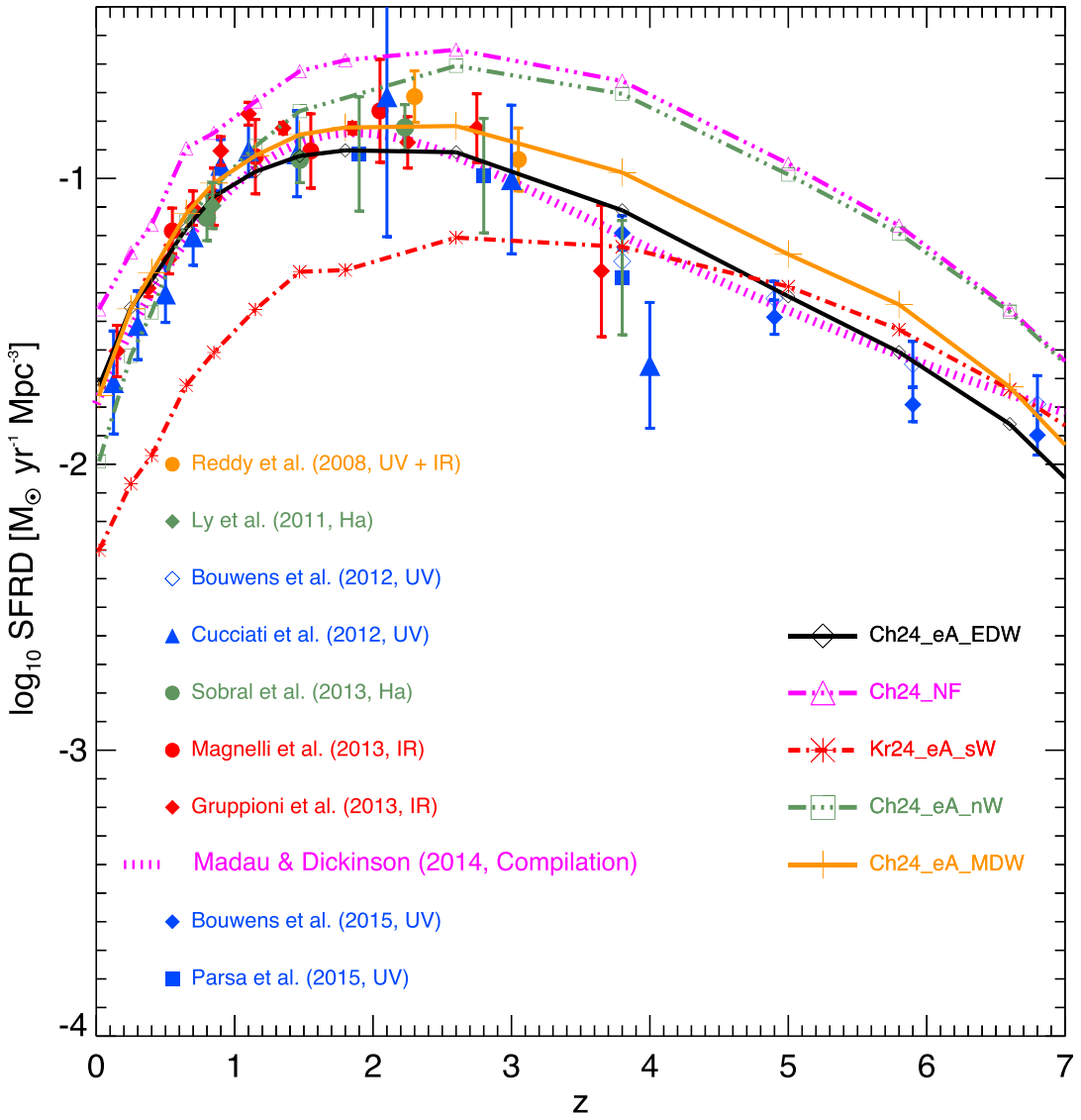

Figure 7. The evolution of the CSFRD from $z \sim 7$ to $z \sim 0$ in cosmological hydrodynamic simulations and observations. The orange filled circles represent the results of Reddy et al. (2008). The red filled reversed triangles, circles and diamonds represent the CSFRD from the integration of the SFRFs implied by the IR LFs of Magnelli et al. (2013) and Gruppioni et al. (2013), respectively. The dark green filled diamonds and green filled circles use the Hα data of Ly et al. (2011) and Sobral et al. (2013), respectively. The blue filled triangles, open diamonds and filled squares represent the CSFRD obtained from UV LFs of Cucciati et al. (2012), Bouwens et al. (2012), Bouwens et al. (2015) and Parsa et al. (2016), respectively. The black dotted line represents the compilation study of Madau & Dickinson (2014). The luminosity limit is set to $L_{\rm min} = 0.03\,L^{\star}$ as in Madau & Dickinson (2014).

supermassive black holes is not sufficient to bring observations and simulations in agreement due to the fact that they are not large enough to produce the required energy to quench the star formation. The presence of another feedback mechanism is required to decrease the simulated CSFRD at $z \geq 1.5$. The *Ch24_eA_EDW* and *Ch24_eA_MDW* runs are implemented with feedback prescriptions that are efficient at high redshifts, making them good candidates. The *Ch24_eA_EDW* run that successfully reproduced the observed SFRF also has an excellent agreement with the constraints from the observed CSFRD. The star formation peak occurs later than in the case with no feedback ($z \sim 2.0$) and has a value 0.3 dex lower. The run with constant energy galactic winds has good agreement with observations at $z \sim 4$–7. However, at $z < 3.5$ it underpredicts the CSFRD with respect to the rest of the simulations. In Section 5, we demonstrated that this feedback prescription is very efficient for objects with high SFRs. In Fig. 7, we see that constant galactic winds are very efficient at low redshifts and decrease the CSFRD substantially. The tension with observations becomes more severe with time (0.3 dex at $z \sim 3.0$, 0.5 dex at $z \sim 1.0$ and 0.7 dex at $z \sim 0$).

In conclusion, the early AGN feedback prescription employed in our model decreases the CSFRD at $z \leq 3$ but is not sufficient to reproduce the observed evolution of the CSFRD at high redshifts ($z \geq 1.5$), since SMBHs are not massive enough to release sufficient energy. Variable galactic winds are perfect candidates to reproduce the observables, since their efficiency is large at high redshifts, but decreases at lower redshifts.

7 CONCLUSIONS

In this paper, we investigated the evolution of the galaxy SFRF at $z \sim$ 1–4. In particular, we have focused on the role of

supernova-driven galactic wind and AGN feedback. We explored the effects of implementations of SN-driven galactic winds presented in Springel & Hernquist (2003), Puchwein & Springel (2013) and Tescari et al. (2014). For the first case, we explored a wind configuration (constant velocity $v_w = 450$). We also adopted variable momentum-driven galactic winds following Tescari et al. (2014) and variable energy-driven galactic winds following Puchwein & Springel (2013).

In the following, we summarize the main results and conclusions of our analysis.

(i) The comparison between the SFRFs from Hα and IR luminosities favour a luminosity/SFR dependent dust correction to the observed Hα luminosities/SFRs. This is in agreement with other authors in the literature (e.g. Hopkins et al. 2001; Cucciati et al. 2012). The IR luminosities provide a good test of dust physics and an appropriate indicator for the intrinsic SFRs. However, these rely on uncertain extrapolation to probe the SFR of low-luminosity star-forming objects. The Hα and UV LFs that are corrected for dust attenuation effects produce SFRFs that are consistent with IR data at intermediate SFRs. Hα and UV SFRF–LFs are able to probe low-mass objects, unlike IR derivations of the SFRF, but are either unable to probe the full population of high SFR objects or the dust correction implied by the IRX–β relation underestimates the amount of dust. This suggests that IR and UV data have to be combined to correctly probe the SFRs of galaxies at both the faint and bright ends of the distribution and that systematic between SFR indicators can affect the measurements of the SFRF. The SFRFs that rely on UV data are shallower than those obtained from IR LFs, with lower characteristic SFRs. Despite their differences at the faint and bright ends of the distribution, UV, Hα and IR SFR indicators are in excellent agreement for objects with $-0.3 \leq \log(\mathrm{SFR}/(\mathrm{M}_\odot\,\mathrm{yr}^{-1})) \leq 1.5$.

(ii) Different SFR indicators produce consistent results for the CSFRD, despite their differences in the faint and bright end of the SFRF. This is most likely due to the fact that all SFR tracers agree well for objects with $-0.3 \leq \log(\mathrm{SFR}/(\mathrm{M}_\odot\,\mathrm{yr}^{-1})) \leq 1.5$, which dominate the CSFRD at $z \sim 1$–4. However, the results from IR SFRFs and LFs are typically 0.10–0.25 dex larger. This is due to the fact that the faint-end slopes of the IR SFRF and LF are not directly constrained by individually detected sources and rely only on extrapolations which have artificially smaller negative slope α. In addition, the characteristic luminosity–SFR of IR studies is higher than that from UV and Hα studies, which are unable to trace dusty systems with high SFRs. Overall, systematics between different SFR indicators do not significantly affect the measurements of the CSFRD, despite the inaccuracies for low- (IR) and high-star-forming systems (UV, Hα).

(iii) The simulation that does not take into account any form of feedback, is consistent with the observed SFRF at the low and intermediate redshifts considered in this work (especially for high-star-forming objects), despite the fact that it is in disagreement with observables at $z > 2.0$. This is a strong indication that in our simulations the efficiency of feedback prescriptions should decrease with time. By construction, variable galactic winds are efficient at decreasing the SFR of objects with low mass. Overall, this prescription should therefore be more efficient at high redshifts where haloes are typically smaller. On the other hand, at low redshifts haloes are typically larger because they had the time to grow through accretion, which results in winds that become less efficient. This behaviour makes variable winds a good choice to model galactic outflows in our simulations.

(iv) The early AGN feedback prescription that we use decreases the CSFRD at $z \leq 3$, but is not sufficient to reproduce the observed evolution of the CSFRD at $z > 3$, since SMBHs are not massive enough to release enough energy at $z \geq 1.5$. On the other hand, variable galactic winds are perfect candidates to reproduce the observables since their efficiency is large at high redshifts and decreases at lower redshifts. The *Ch24_eA_EDW* run is the simulation that performs best overall.

In conclusion, we favour galactic winds that produce feedback that becomes less efficient with time. We favour feedback prescriptions that decrease the number of objects with low SFRs.

ACKNOWLEDGEMENTS

We would like to thank Volker Springel for making available to us the non-public version of the GADGET-3 code. We would also like to thank Stuart Wyithe, Kristian Finlator, Lee Spitler and the anonymous referee for their comments. This research was conducted by the Australian Research Council Centre of Excellence for All-sky Astrophysics (CAASTRO), through project number CE110001020. This work was supported by the NCI National Facility at the ANU, the Melbourne International Research Scholarship (MIRS) and the Albert Shimmins Fund – writing-up award provided by the University of Melbourne. AK is supported by the CONICYT-FONDECYT fellowship (project number: 3160049).

REFERENCES

Alavi A. et al., 2014, ApJ, 780, 143
Barai P. et al., 2013, MNRAS, 430, 3213
Bell E. F., Zheng X. Z., Papovich C., Borch A., Wolf C., Meisenheimer K., 2007, ApJ, 663, 834
Bouwens R. J., Illingworth G. D., Franx M., Ford H., 2007, ApJ, 670, 928
Bouwens R. J. et al., 2009, ApJ, 705, 936
Bouwens R. J. et al., 2012, ApJ, 754, 83
Bouwens R. J. et al., 2015, ApJ, 803, 34
Calzetti D. et al., 2007, ApJ, 666, 870
Cucciati O. et al., 2012, A&A, 539, A31
Davé R., Oppenheimer B. D., Finlator K., 2011, MNRAS, 415, 11
Dolag K., Stasyszyn F., 2009, MNRAS, 398, 1678
Dolag K., Jubelgas M., Springel V., Borgani S., Rasia E., 2004, ApJ, 606, L97
Dolag K., Grasso D., Springel V., Tkachev I., 2005, J. Cosmol. Astropart. Phys., 1, 9
Dole H. et al., 2006, A&A, 451, 417
Draine B. T., Li A., 2007, ApJ, 657, 810
Elbaz D., Hwang H. S., Magnelli B., Daddi E. et al., 2010, A&A, 518, L29
Fabjan D., Borgani S., Tornatore L., Saro A., Murante G., Dolag K., 2010, MNRAS, 401, 1670
Fontanot F., Cristiani S., Santini P., Fontana A., Grazian A., Somerville R. S., 2012, MNRAS, 421, 241
Gallego J., Zamorano J., Aragon-Salamanca A., Rego M., 1995, ApJ, 455, L1
Glazebrook K., Blake C., Economou F., Lilly S., Colless M., 1999, MNRAS, 306, 843
Gruppioni C. et al., 2013, MNRAS, 432, 23
Hanish D. J. et al., 2006, ApJ, 649, 150
Hao C.-N., Kennicutt R. C., Johnson B. D., Calzetti D., Dale D. A., Moustakas J., 2011, ApJ, 741, 124
Hayes M., Schaerer D., Östlin G., 2010, A&A, 509, L5
Helou G., 1986, ApJ, 311, L33
Hirashita H., Buat V., Inoue A. K., 2003, A&A, 410, 83
Hopkins A. M., Connolly A. J., Szalay A. S., 2000, AJ, 120, 2843
Hopkins A. M., Connolly A. J., Haarsma D. B., Cram L. E., 2001, AJ, 122, 288

Iannuzzi F., Dolag K., 2011, MNRAS, 417, 2846
Katsianis A., Tescari E., Wyithe J. S. B., 2015, MNRAS, 448, 3001
Katsianis A., Tescari E., Wyithe J. S. B., 2016, PASA, 33, e029
Kennicutt R. C., Jr,1983, ApJ, 272, 54
Kennicutt R. C., Jr,1998a, ARA&A, 36, 189
Kennicutt R. C., Jr,1998b, ApJ, 498, 541
Kewley L. J., Geller M. J., Jansen R. A., 2004, AJ, 127, 2002
Le Floc'h E. et al., 2005, ApJ, 632, 169
Ly C., Lee J. C., Dale D. A., Momcheva I., Salim S., Staudaher S., Moore C. A., Finn R., 2011, ApJ, 726, 109
Madau P., Dickinson M., 2014, ARA&A, 52, 415
Madau P., Pozzetti L., Dickinson M., 1998, ApJ, 498, 106
Magnelli B., Elbaz D., Chary R. R., Dickinson M., Le Borgne D., Frayer D. T., Willmer C. N. A., 2011, A&A, 528, A35
Magnelli B. et al., 2013, A&A, 553, A132
Maio U., Tescari E., 2015, MNRAS, 453, 3798
Maio U., Dolag K., Ciardi B., Tornatore L., 2007, MNRAS, 379, 963
Martin C. L., 2005, ApJ, 621, 227
Meurer G. R., Heckman T. M., Calzetti D., 1999, ApJ, 521, 64
Moorwood A. F. M., van der Werf P. P., Cuby J. G., Oliva E., 2000, A&A, 362, 9
Moustakas J., Kennicutt R. C., Jr, Tremonti C. A., 2006, ApJ, 642, 775
Oesch P. A. et al., 2010, ApJ, 725, L150
Parsa S., Dunlop J. S., McLure R. J., Mortlock A., 2016, MNRAS, 456, 3194
Pérez-González P. G., Zamorano J., Gallego J., Aragón-Salamanca A., Gil de Paz A., 2003, ApJ, 591, 827
Pettini M., Kellogg M., Steidel C. C., Dickinson M., Adelberger K. L., Giavalisco M., 1998, ApJ, 508, 539
Planelles S., Borgani S., Dolag K., Ettori S., Fabjan D., Murante G., Tornatore L., 2013, MNRAS, 431, 1487
Puchwein E., Springel V., 2013, MNRAS, 428, 2966
Reddy N. A., Steidel C. C., 2009, ApJ, 692, 778
Reddy N. A., Steidel C. C., Pettini M., Adelberger K. L., Shapley A. E., Erb D. K., Dickinson M., 2008, ApJS, 175, 48
Rex M. et al., 2010, A&A, 518, L13
Rujopakarn W., Rieke G. H., Eisenstein D. J., Juneau S., 2011, ApJ, 726, 93
Salpeter E. E., 1955, ApJ, 121, 161
Schechter P., 1976, ApJ, 203, 297
Smit R., Bouwens R. J., Franx M., Illingworth G. D., Labbé I., Oesch P. A., van Dokkum P. G., 2012, ApJ, 756, 14
Sobral D., Smail I., Best P. N., Geach J. E., Matsuda Y., Stott J. P., Cirasuolo M., Kurk J., 2013, MNRAS, 428, 1128
Springel V., 2005, MNRAS, 364, 1105
Springel V., Hernquist L., 2003, MNRAS, 339, 289
Springel V. et al., 2005, Nature, 435, 629
Sullivan M., Treyer M. A., Ellis R. S., Bridges T. J., Milliard B., Donas J., 2000, MNRAS, 312, 442
Tacchella S., Trenti M., Carollo C. M., 2013, ApJ, 768, L37
Teplitz H. I. et al., 2000, ApJ, 542, 18
Tescari E., Katsianis A., Wyithe J. S. B., Dolag K., Tornatore L., Barai P., Viel M., Borgani S., 2014, MNRAS, 438, 3490
Tornatore L., Ferrara A., Schneider R., 2007a, MNRAS, 382, 945
Tornatore L., Borgani S., Dolag K., Matteucci F., 2007b, MNRAS, 382, 1050
Tresse L., Maddox S. J., Le Fèvre O., Cuby J.-G., 2002, MNRAS, 337, 369
van der Burg R. F. J., Hildebrandt H., Erben T., 2010, A&A, 523, A74
Wiersma R. P. C., Schaye J., Smith B. D., 2009, MNRAS, 393, 99
Yan H., Windhorst R. A., Cohen S. H., 2003, ApJ, 585, L93

This paper has been typeset from a TEX/LATEX file prepared by the author.